NASA Contractor Report 4391

Three-Dimensional Compressible Turbulent Computations for a Nondiffusing S-Duct

G. J. Harloff, J. R. DeBonis,
C. F. Smith, and J. E. Bruns

CONTRACT NAS3-25266
APRIL 1992

NASA

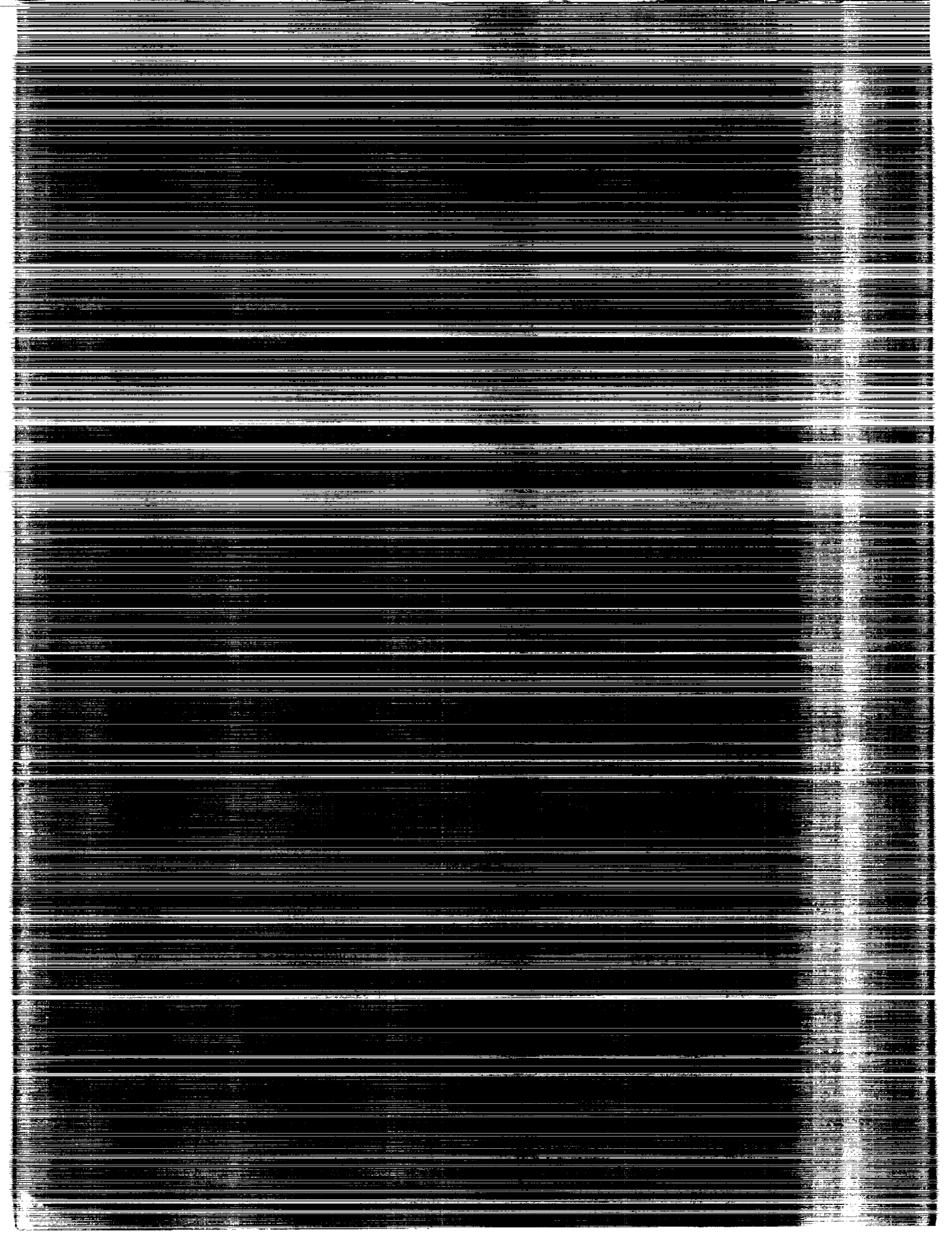

NASA Contractor Report 4391

Three-Dimensional Compressible Turbulent Computations for a Nondiffusing S-Duct

G. J. Harloff, J. R. DeBonis,
C. F. Smith, and J. E. Bruns
Sverdrup Technology, Inc.
Lewis Research Center Group
Brook Park, Ohio

Prepared for
Lewis Research Center
under Contract NAS3-25266

National Aeronautics and
Space Administration

Office of Management

Scientific and Technical
Information Program

1992

Summary

The PARC3D code was used to compute the compressible turbulent flow within a three-dimensional nondiffusing S-duct. The present study provides a frame of reference for future computational fluid dynamic studies of internal flows with strong secondary flows and provides an understanding of the performance characteristics of a typical S-duct with attached flow. The predicted results, obtained with both H- and O-grids, are compared with the experimental wall pressures, static- and total-pressure fields, and velocity vectors. Additionally, computed boundary-layer thickness, velocity profiles in wall coordinates, and skin friction values are presented.

Introduction

Many aircraft have curved rectangular and circular duct geometries in the inlet and exhaust of their propulsion systems. The flow within these ducts may have strong secondary elements. Examples of aircraft with inlet S-ducts are the Boeing 727, the Lockheed Tristar (L-1011), the General Dynamics F-16, and the McDonnell-Douglas F-18. The performance of these types of ducts is usually determined by wind tunnel testing. Recently, computational fluid dynamic (CFD) capabilities have improved, and both parabolized and full Navier-Stokes computer programs are used to predict the flows in these ducts.

The present study was conducted to evaluate the capabilities of a computational fluid dynamics computer program to model the flow physics and performance characteristics of a three-dimensional nondiffusing subsonic S-duct with moderate to high subsonic flow conditions. The flow processes in the three-dimensional geometry induce secondary flow. The full three-dimensional Navier-Stokes equations have been solved with the PARC3D (ref. 1) code together with an algebraic turbulence model for closure. In contrast to previously published work, the current study permits the inlet mass flow to adjust to the interior flow field. The entrance velocity and static-pressure fields adjust to the duct geometry and the flow losses. Solutions were obtained for H- and O- grids in order to examine the grid effects on the solution. The inviscid contributions to the secondary flow field were quantified by solving the Euler equations for irrotational and rotational inflow. This study provides a basis to evaluate the computer program and provides an understanding of the performance characteristics of a nondiffusing S-duct.

The literature review in the appendix shows the state of the art in modeling these kinds of flows. Recommendations are made for further work in the modeling of these ducts.

Symbols

A	sublayer thickness
A^+	AU_t/ν
C_f	skin friction coefficient
C_{ps}	static-pressure coefficient, $(P_s - P_{s,\mathrm{ref}})/Q_{\mathrm{ref}}$
C_{pt}	total-pressure coefficient, $(P_t - P_{s,\mathrm{ref}})/Q_{\mathrm{ref}}$
D	diameter
P_s	static pressure
P_t	total pressure
Q	dynamic pressure
Re	Reynolds number, $\rho_{\mathrm{ref}} u_{\mathrm{ref}} D/\mu$
S	arc length along centerline of duct
T_w	wall shear stress
U^+	$= U/U_t$
U_t	friction velocity, $\sqrt{\lvert T_w \rvert/\rho_w}$
u	velocity in x direction
U_e	edge velocity in x direction
v	velocity in y direction
w	velocity in z direction
x	coordinate distance
y	coordinate distance
Y^+	yU_t/ν
z	coordinate distance

δ boundary-layer thickness

ν kinematic viscosity

ρ density

ϕ circumferential angular position around duct

Subscripts:

l laminar

ref reference station (station I)

t turbulent

w wall

Description of the Test Data

The experiment of Vakili et al. (ref. 2) is modeled in the present study. The duct had a circular, constant-area cross section with two 30° bends (fig. 1). The duct was designed to avoid streamwise flow separation. A straight pipe of 30 in. was connected to a duct exit (not shown) to provide the flow and turbulent boundary layers for the upstream bend of the S-duct. The inlet boundary layer was turbulent, and its thickness was about 7.8 percent of the 3.25-in. duct inside radius. The average inlet Mach number was 0.6. The inside duct diameter was 6.5 in., and the radius of curvature R of 33 in. was about 5 diameters (see fig. 1). The duct vertical offset was about 1 diameter. A straight, 60-in.-long section, installed downstream of the S-duct, conducted the flow to the exit (ambient air). The Reynolds number was 3.25×10^6 per foot.

Vakili et al. (ref. 2) measured wall static-pressures along three azimuth angles, ϕ, of 0° (top), 90°, and 180° (bottom) (see fig. 1(a)) and total-pressure profiles at six axial measurement stations (including a reference station) (see fig. 1(b)). They also measured the static-pressure field and computed flow velocity from the static and total pressures. These experimental data are to be compared with computed results herein.

Computer Program

The PARC3D (ref. 1) computer program solves the full, three-dimensional, Reynolds-averaged, Navier-Stokes equations in strong conservation form with the Beam and Warming (ref. 3) approximate factorization algorithm. The implicit scheme uses central differencing and generalized coordinates. The code was originally developed as AIR3D by Pulliam and Steger (ref. 4); Pulliam later added the Jameson type of artificial dissipation (ref. 5) and called the code ARC3D (ref. 6). Cooper adapted the ARC3D code for internal propulsion application and named the code PARC3D (ref. 1).

Grid

The cross-sectional shape of an aircraft duct often changes from rectangular to circular, or vice-versa. Therefore, one type of grid may not fit the boundaries throughout the duct. An H-grid conforms well to a rectangular shape, and an O-grid conforms to a circular cross section. One problem with the O-grid is that the pole boundary condition at the center of the grid is an average of the surrounding flow properties. A problem with the H-grid is that it may not conform well to a curved boundary, for example, the "corner points" (see fig. 2(a)) of the grid exhibit excessive skewing. The proper choice of grid can be illusive for a transitioning duct. In this study the effects on the numerical solutions using both H-grid and O-grids were investigated to provide insight into numerical differences. The H-grid dimensions (fig. 2(a)) are 75 by 33 by 33, and the O-grid dimensions (fig. 2(b)) are 75 by 35 by 31 in the streamwise, circumferential, and radial directions, respectively. The upstream and downstream lengths of straight duct are the same for both grids. The H-grid for the S-duct was generated using the INGRID3D code (ref. 7). An algebraic approach was used to obtain the initial H-grid, and this grid was then smoothed using an elliptic equation solver.

The grid distributions were developed based on two criteria: First, the maximum number of grid points, consistent with the Cray resources available, was used and, second, the wall spacing for the first grid point of the H-grid was as close as the grid generation computer program could compute it (due to grid skewness limitations on cell size). The O-grid was developed considering the pole boundary condition and reasonable wall spacing.

Boundary Conditions

The boundary conditions used were no slip on the walls, zero gradients along the plane of symmetry, total-pressure and temperature conditions specified at the entry plane, and static pressure specified at the exit plane. The O-grid used a pole average boundary condition, with a radius less than 1 percent of the duct radius. The entrance velocity and static-pressure were permitted to change by averaging an incoming and an extrapolated interior Riemann invariant.

Turbulence Model

The Baldwin-Lomax (ref. 8) algebraic turbulence model was used to model turbulence. The wall weighing logic for the H-grid used the minimum of the two values of

eddy viscosity, calculated at a point, due to each wall (fig. 2(a)). The O-grid turbulent viscosities used only one value at each radial and angular position, since only one wall, or radial distance, is present.

Results and Discussion

Euler Solutions with Irrotational and Rotational Inflow: Static Pressure

In order to investigate the inviscid contributions to the secondary flow and to examine the magnitude of the viscous effects, the Euler equations were solved for irrotational and rotational inflow conditions using an O-grid. For both the irrotational and rotational flow cases, the downstream pressure was adjusted to obtain the same mass flow at the inflow boundary. An incoming uniform flow was used for the irrotational flow case. For the rotational flow case the upstream conditions, at the duct reference station (station I), were held fixed, and the interior flow was computed without viscosity, that is, the flow was considered inviscid. The fixed inflow conditions were computed by the fully viscous calculations discussed below. In the viscous calculations presented below the inlet mass flow was determined as part of the solution.

The computed surface static-pressures for the irrotational and rotational flow cases are shown in figures 3(a) and (b) using the O-grid results. The general trends of these profiles are similar, which implies that the streamwise pressure gradients are determined primarily by irrotational effects. The experimental pressures should not and do not agree with either of these two approximations, as there are no total-pressure losses in either of them. (PNS solutions generally impose a fixed pressure field based on these inviscid assumptions.) The effects of the inlet vorticity on the total-pressure and secondary-flow fields are discussed in the section on viscous effects below.

Fully Viscous Solution

Static pressure.—The surface static-pressure distributions obtained from the O- and H-grid solutions are compared with the measured distribution in figures 3(c) and (d). Both solutions provide reasonable agreement with the test data and, because of to the computed overall total-pressure loss, are considerably improved over the inviscid flow computations discussed above.

Comparisons of the experimental static-pressure coefficient contours and those obtained using O- and H-grids are shown in figure 4. The O- and H-grid pressure fields are in reasonable agreement with each other and are different in shape from the experimental fields. However, the levels are similar, except at station V (fig. 4(e)) where the experimental contours might be mislabeled. For example, the wall static values at an *S/D* of 4 (figs. 3(c) and (d)) differ from the values close to the wall (fig. 4(e)). This discrepancy in pressure should be further investigated in any additional experimental testing of this S-duct. Another possible explanation is that the algebraic turbulence model used does not properly account for the secondary flow effects or for the imbedded vorticity effects. This is consistent with recent findings of Monson et al. (ref. 9) and current Stanford research (personal communication from P. Bradshaw of Stanford). The experimental static-pressure field might be indicative of a strong secondary flow field even at the reference station (station I).

Total pressures.—Total-pressure contours are compared in figure 5 for the six measurement stations. In general, agreement is very good between the O-grid and H-grid solutions, and the numerical results are in reasonable agreement with the experimental total-pressure contours. The secondary flow develops very rapidly in the second bend. This can be observed by comparing the total-pressure contours at stations III and IV (figs. 5(c) and (d)) with stations V and VI (figs. 5(e) and (f)). It is not clear why the numerical results do not agree with experimental contours at (the bottom of) station III (fig. 5(c)). This disagreement may be attributed to the change in the static-pressure gradient, which, in the second bend, tends to reinforce the secondary flow development. For example, in the first bend (see fig. 6) the region of high static-pressure is at the top of the duct ($\phi = 0°$), which tends to cause fluid to accumulate near the wall. In the second bend the higher static-pressure is at the bottom of the duct ($\phi = 180°$), which tends to push the flow away from the walls.

Two anomalies in the experimental data have been noticed. In the contours at station IV (fig. 5(d)), two disturbances are observed in the data. One is near $\phi = 0°$ (top), and one is near $\phi = 180°$ (bottom). The disturbance near $\phi = 180°$ is due to the presence of an upstream probe (personal communication from A. Vakili). The disturbance at the top of the duct is of unknown origin. The computed results at station VI (fig. 5(f)) indicate that the computed secondary flow is not as strong as the actual secondary flow. This discrepancy may be due to secondary flow and vorticity effects not being properly accounted for in the turbulence modeling. Another possibility is that the discrepancy may be due to boundary-layer resolution issues due to inadequate grid spacing near the wall. The Y^+ distance of the first grid point off the wall is approximately 19 for the O-grid, which is in the buffer layer of the boundary layer. The first grid point should be closer to the wall for better boundary-layer resolution.

Velocity vectors.—The computed velocity vectors for the two grids are compared with the experimental data in figure 6, with reasonable qualitative agreement. The distorted velocity vectors in the H-grid solution indicate the presence of some noise in the solution in the regions of the

corners of the computational grid, which is attributed to the very large amounts of grid skewness in these corner regions. The overall solution does not appear to be affected by this skewness. The magnitude of the computed velocity vectors is smaller than the experimental data, which is consistent with the previously mentioned observations that the secondary flow is underpredicted.

Boundary layers.—Experimental and predicted boundary-layer thickness is plotted versus distance in figure 7. Good agreement between the predicted and experimental values is shown. The boundary-layer thicknesses are defined as the perpendicular distance from the wall where the total-pressure coefficient, C_{pt}, is 1.025. Flat-plate boundary-layer thickness is shown for comparison. A rapid increase in the boundary-layer thickness, δ, occurs along the 180° surface at an *S/D* of approximately 2. The boundary-layer thickness on the 0° (top) surface grows at the next highest rate and on the 90° (side) surface grows very similar to that of a flat plate. This rapid growth behavior is due to the movement of the fluid away from the wall by the strong secondary flow (see figs. 5(d) and (e) and 6(c) and (e)). The computed reference station velocity profile is similar to the 1/7th power law for the O- and H-grids, as shown in figure 8.

Turbulent viscosity levels are shown in figure 9 for the O- and H-grids, respectively, just upstream of the S-duct at the station I (fig. 1(b)). The H- and O-grid turbulent viscosities are symmetric. The H-grid turbulent viscosities drop to zero on the centerline because of the minimization of the turbulent viscosity values from the two walls in the computer code (see the **Turbulence Model** section).

The O-grid velocity profiles, in wall coordinates (e.g., U^+ vs. Y^+), are shown in figure 10 for the stations I, IV, and VI. The data are also shown in the figure. The H-grid results are shown in figure 11 for stations I, IV, and VI. The friction velocity U_t (see table I), which is used to normalize both the computational and the experimental results, was obtained by a successive substitution procedure, which forced one of the points to fit on the law of the wall (ref. 10). The law of the wall used was $U^+ = U/U_t = 5.6 \log Y^+ + 4.9$, which is for a flat plate; the intercept for a round pipe is 5.5. The flat-plate formulation (without pressure gradient effects) is adequate for this analysis. The first experimental data point was quite high in the boundary layer, about 1000 Y^+ and was assumed to be in the linear region. This procedure was applied to both the computational and experimental data because the first points were not in the linear sublayer and thus a good friction velocity could not be directly computed. The shear velocities for the O-grid and the experimental data are listed in table I. Qualitatively, the experimental data and the computational results show the same trends. A difference might be due to the fact that the experimental point is so far from the boundary (Y^+ of 1000).

TABLE I.—FRICTION VELOCITY USED TO NORMALIZE VELOCITY AND C_f

Station	Axial position	Friction velocity, U_t, ft/sec	Edge velocity, U_e, ft/sec	Velocity ratio, U_t/U_e
O-grid calculation				
I (reference)	0	17.263	545	0.0317
	90	17.241	545	.0316
	180	17.272	545	.0317
IV	0	18.282	574	0.0318
	90	18.111	574	.0316
	180	11.421	574	.0199
VI	0	15.923	584	0.0273
	90	17.581	584	.0301
	180	15.632	584	.0268
Experiment (computed based on linear log wall fit)				
I	0	21.769	568	0.0383
	100	18.975	546	.0348
	180	20.744	560	.0370
IV	0	26.126	600	0.0435
	100	22.435	620	.0362
	180	13.474	636	.0212
VI	0	21.117	600	0.0352
	100	24.593	610	.0403
	180	21.231	628	.0338

The computed shear stress divided by the reference dynamic pressure is the local skin friction coefficient. The wall shear stress is computed from the derived friction velocity, U_t. Shear stress is shown for both the O- and H-grids as a function of axial distance for $\phi = 0°$, 90°, and 180° in figure 12. The comparison of C_f for both grids provides a measure of the grid dependence of the results. The O-grid flow field was used to obtain contours of wall C_f along the duct surface (see fig. 12(b)). The C_f values computed from measured velocities are in qualitative agreement with the full Navier-Stokes analysis values. Note that experimentally determined C_f values were not available.

Viscous Effects: Total Pressure and Secondary Flow

To determine the viscous effects on the total-pressure and secondary-velocity fields, a study was conducted where the interior flow was assumed to be inviscid and the entrance velocity profile was fixed with the viscous inlet flow field. The results, shown in figures 13 and 14, can be directly compared with the fully viscous results shown in figures 5 and 6. The two counterrotating vortices are evident at the exit station (see figs. 13(f) and 14(e)). The vortex strength is, however, significantly weaker than the experiment. The secondary flow is driven by the inviscid

pressure field. However, the absence of vorticity generation at the wall reduces the strength of the secondary flow.

Vorticity Contours

Classical theories (see, e.g., Squire and Winter (ref. 11)) attribute the origin of secondary flows in ducts to the lateral deflection of the transverse vorticity component present in the incoming boundary layer. (The appendix summarizes the available literature.) Vortex stretching results in the generation of counterrotating vortices. The irrotational flow results, which are not presented, showed no secondary flow development and were consistent with these theories. Contours of streamwise vorticity are shown in figure 15 for inviscid flow (with rotational inflow) and in figure 16 for fully turbulent flow. As can be seen in the figures, the inviscid rotational inflow accounts for a significant portion of the secondary flow present for the fully viscous case.

In the inviscid-rotational case the vorticity profile is nearly symmetric at station IV, (duct inflection point) and looks similar to the fully viscous calculation (see fig. 16). At the duct exit the vortices are much larger and weaker (compare figs. 16 and 15) for the fully viscous case.

Concluding Remarks

The computed total pressures are generally in good agreement with the experimental data, and the velocity vectors are in qualitative agreement with the test data. Both the H- and the O-grids resulted in similar flow fields, with the O-grid providing higher quality turbulent viscosities because of its lack of grid corner effects, as discussed in the report. The predicted static-pressures were in reasonable agreement with measurements. The two counterrotating vortices at the S-duct exit were predicted. The rotational Euler solutions show that the development of the secondary flows in S-ducts is partially driven by inviscid phenomena, provided a velocity profile enters the diffuser.

The modeling could be improved by using adaptive gridding techniques and more advanced turbulence models. Grid refinement might improve the agreement between calculations and experiment, with the first grid point in the sublayer, for example, Y^+ of 1 to 5. The complete duct length should be modeled because of the importance of vorticity generation effects. Additional fundamental experimental and numerical studies are necessary to properly address the turbulence modeling issues with imbedded vortices and strong secondary flows.

Turbulence modeling issues include wall weighing strategy, adequacy of existing algebraic, k-ε, and algebraic Reynolds stress models in flows with strong cross flows and imbedded vorticity, and finally the adequacy of wall functions for strong secondary flows.

Because of a lack of suitable compressible CFD validation data (see appendix), additional comprehensive experimental data that should be obtained. It is recommended that the following three ducts be built and tested:

1. The S-duct examined herein to take advantage of advanced instrumentation and measurement techniques (laser Doppler velocimetry, for example)
2. A diffusing transition duct, rectangular to round
3. A typical engine duct.

Input velocity profile should be a test variable, including an asymmetric profile. Detailed flow surveys are needed to assess turbulence models and grid adequacy issues. The computed results presented herein should be used as a "template" for locations to obtain test data. It is recommended that laser Doppler anemometry and hot-wire measurements be obtained to provide high quality velocity profiles and turbulent shear stress distributions beginning at $Y^+ = 10$. Skin friction values are also needed to compare with existing predictions. A thorough comparison of the experimental and (existing and future) computed turbulence shear stress values should provide information regarding the adequacy of the turbulence models for flows with strong secondary flows. Additional work will be needed to define the components of the shear stress distributions from the computed velocity field results, and additional turbulence models should be used, as necessary, to compute the turbulent Reynolds stresses.

Appendix A — Literature Review

The literature was reviewed to determine the status of experiment data and the state of the art in modeling these kinds of flows. Recommendations are made for further work in the modeling of these ducts.

Experiments

Bansod and Bradshaw (ref. 12) conducted experiments on three constant-area S-ducts. The flow was incompressible with a Reynolds number, based on diameter, of 0.5×10^6. The streamwise deflection of the boundary layer in the first bend produced streamwise vorticity. A pair of vortices formed at the outside (radius) of the second bend and caused the boundary-layer thickness to increase rapidly. Willmer et al. (ref. 13) tested a circular inlet and an S-duct at Mach numbers from 0 to 0.21 and at incidence and sideslip angles from 0° to 40°. Losses at the engine face were determined as a function of lip shape, contraction area ratio, boundary-layer transition location, lip slot, and offset diffuser. Guo and Seddon (ref. 14) experimentally investigated the incompressible flow in a constant area rectangular S-duct mounted in a wind tunnel. The ducts had two 35° bends, and tests were conducted to an angle of attack of 30° and to an angle of yaw of 10°. The Reynolds number, based on diameter, varied from 2.1 to 2.7×10^5. Total-pressure contours, recovery, and turbulence levels were reported. Flow separation, large exit flow distortion, a pair of counterrotating vortices, and high turbulence levels were observed. McMillan (ref. 15) tested a diffusing duct of 40° to obtain incompressible CFD validation data. A pair of counterrotating streamwise vortices dominated the flow. Schmidt (ref. 16) et al. conducted experiments to provide incompressible CFD validation data for a rectangular constant-area duct with S-ducts upstream and downstream. The Reynolds numbers tested were 790 and 40 000 based on hydraulic diameter. A second duct was tested with a circular cross section and a 45° uniform-area S-duct upstream and a 22.5° and 22.5° downstream S-duct diffuser.

Numerical Analyses

Rowe (ref. 17) provided early experiments and inviscid computations of flow in a 45° S-bend and a 180° pipe, with a Reynolds number of 2.36×10^5, based on diameter. He solved the continuity equation in the cross plane for the secondary flow and solved a Poisson equation with the vorticity source term to determine the secondary flow velocities. Towne and Anderson (ref. 18) conducted a numerical study with a PNS computer program of a circular S-duct. The incompressible flow Reynolds number was 2000, based on diameter. They also analyzed the F-16 inlet duct, with an elliptical inlet shape and round exit with an area ratio of 1.3. A turbulent flow calculation was completed with Reynolds number of 1.44×10^7 and an entrance Mach number of 0.9; the inlet flow field was specified. Good agreement with exit total-pressure data was obtained. Vakili et al. (ref. 19) reported experimental and computational results for a 30° to 30° nondiffusing S-duct, the nondiffusing duct analyzed in this paper. The inlet Mach number was 0.6, the Reynolds number was 3.25×10^6 per foot and the inlet boundary layer was 0.078 of the duct radius. The parabolized Navier-Stokes (PNS) computation agreed well with the experimental total pressures and velocity vectors. Towne (ref. 20) used a PNS code to predict the total-pressure field for several RAE inlet ducts with offsets of 0.3 and 0.45, with and without centerbody hubs. Predicted total-pressure profiles were in good agreement with experiment results.

Malechi and Lord (ref. 21) used a PNS code to calculate the flow field of two circular to rectangular transition ducts. These ducts produced a pair of counterrotating vortices like those of S-ducts. The authors concluded it was important to have accurate inlet boundary-layer profiles in order to accurately calculate the (fixed) input static-pressure field necessary for the PNS solution. The PNS solver underpredicted the vortex strength and the cross-sectional velocities. They used the *k-e* turbulence model, and they concluded that the turbulent eddy viscosity was (numerically) suppressed in the vortex core. Cosner (ref. 22) reported a FNS simulation of a compact highly offset diffuser with an inlet Mach number of 0.777. The boundary layer separated from the inner bend of the diffuser at half the diffuser length. Predictions were also made for a different diffuser with an assumed uniform inflow (with a boundary layer) at Mach number 0.65. Static-pressure and boundary-layer profiles were not presented, nor were grid and turbulence model details.

Monson et al. (refs. 9 and personal communication with D.J. Monson, Feb. 1990) compared experimental data and full Navier-Stokes (FNS) numerical results for a rectangular (space shuttle main engine), 180° U-duct. The Mach number was 0.1, and the Reynolds numbers, based on channel height, were 10^5 and 10^6. They concluded that simple mixing length models are inadequate for strong secondary flows.

Conclusions From the Literature

Vortex pairs are evident in the exit planes of S-ducts, transition ducts, and bending rectangular ducts. These vortices are due to secondary flows induced by pressure gradients. Benchmark CFD validation data exist for incompressible flow. The Vakili (refs. 2 and 19) data are among the few sets of compressible CFD validation data available. Therefore, a need exists for additional experimental data for code validation with strong crossflow. A possible limitation of both algebraic and *k-e* turbulence modeling for strong secondary flows has been noted by several researchers.

The mechanism that produces the low total-pressure region at the exit is an inviscid rotational phenomenon, provided an inlet boundary layer is present. This obviously requires correct inlet boundary conditions. The previous computational investigations appear to be limited to FNS or PNS computations, which did not account for the upstream effect of mass flow adjustment, boundary-layer growth, and flow blockage, that is, the published solutions have specified inlet conditions. The PNS solutions usually rely on an input inviscid static-pressure field, which is generally from an Euler or irrotational analysis. (Most PNS solvers are single pass and do not iterate on pressure). The interior static-pressure fields for these calculations have not been presented, thus, it is difficult to assess the accuracy of the complete flow field solution, especially in terms of secondary flow or exit velocity.

References

1. Cooper, G.K.: The Parc Code: Theory and Usage. AEDC-TR-87-24, Oct. 1987. (Avail. NTIS, AD-B115169.)
2. Vakili, A.; Wu, J.M.; Liver, P.; and Bhat, M.K.: An Experimental Investigation of Secondary Flows in a S-Shaped Circular Duct. UTSI 83108, University of Tennessee Space Institute, 1983.
3. Beam, R.M.; and Warming, R.F.: An Implicit Factored Scheme for the Compressible Navier-Stokes Equations. AIAA J., vol. 16, no. 4, Apr. 1978, pp. 393-402.
4. Pulliam, T.H.; and Steger, J.L.: Implicit Finite-Difference Simulations of Three Dimensional Compressible Flow. AIAA J., vol. 18., no. 2, Feb. 1980, pp. 159-167.
5. Jameson, A.; Schmidt, W.; and Turkel, E.: Numerical Solutions of the Euler Equations by Finite Volume Methods Using Runge-Kutta Time-Stepping Schemes. AIAA Paper 81-1259, June 1981.
6. Pulliam, T.H.: Euler and Thin Layer Navier-Stokes Codes: ARC2D, ARC3D. Notes for Computational Fluid Dynamics User's Workshop, The University of Tennessee Space Institute, Tullahoma, TN, UTSI Pub. E02-4005-023-84, 1984, pp. 15.1-15.85.
7. Dorrell, E.W.; and McClure, M.D.: 3D INGRID: Interactive Three-Dimensional Grid Generation. AEDC-TR-87-40, Apr. 1988. (Avail. NTIS, AD-B121739L.)
8. Baldwin, B.S.; and Lomax, H.: Thin Layer Approximation and Algebraic Model for Separated Turbulent Flows. AIAA Paper 78-257, Jan. 1978.
9. Monson, D.J.; Seegmiller, H.L.; and McConnaughey, P.K.: Comparison of LDV Measurements and Navier Stokes Solutions in a Two-Dimensional 180-degree Turn-Around Duct. AIAA Paper 89-0275, Jan. 1989.
10. Coles, D.: The Law of the Wake in the Turbulent Boundary Layer. J. Fluid Mech., vol. 1, pt. 2, July 1956, pp. 191-226.
11. Squire, M.B.; and Winter, K.G.: The Secondary Flow in a Cascade of Airfoils in a Nonuniform Stream. J. Aeronaut. Sci., vol. 18, no. 4, Apr. 1951, pp. 271-277.
12. Bansod, P.; and Bradshaw, P.: The Flow in S-Shaped Ducts. Aeronaut. Q., vol. 23, May 1972, pp. 131-140.
13. Willmer, A.C.; Brown, T.W.; and Goldsmith, E.L.: Effects of Intake Geometry on Circular Pitot Intake Performance at Zero and Low Forward Speeds. Aerodynamics of Power Plant Installations, AGARD, Neuilly-Sur-Seine, France, 1981, pp. 5-1 to 5-16.
14. Guo, R.W.; and Seddon, J.: An Investigation of the Swirl in an S-Duct. Aeronaut. Q., vol. 33, Feb. 1982, pp. 25-58.
15. McMillan, O.J.: Mean-Flow Measurements of the Flow Field in a Diffusing Bend. NASA CR-3634, 1982.
16. Schmidt, M.C.; Whitelaw, J.H.; and Yianneskis, M.: Flow in Out-of-Plane Double S-Bends. NASA CR-176981, 1986.
17. Rowe, M.: Measurements and Computations of Flow in Pipe Bends. J. Fluid Mech., vol. 43, pt. 4, Oct. 2, 1970, pp. 771-783.
18. Towne, C.E.; and Anderson, B.H.: Numerical Simulation of Flows in Curved Diffusers With Cross-Sectional Transitioning Using a Three-Dimensional Viscous Analysis. NASA TM-81672, 1981.
19. Vakili, A., et al.: Comparison of Experimental and Computational Compressible Flow in a S-Duct. AIAA Paper 84-0033 Jan. 1984.
20. Towne, C.E.; and Flitcroft, J.E.: Analysis of Intake Ducts Using a Three-Dimensional Viscous Marching Procedure. Presented at the First World Congress on Computational Mechanics, Austin, TX, Sept. 1986.
21. Malecki, R.E.; and Lord, W.K.: Parabolized Navier-Stokes Analysis of Circular-to-Rectangular Transition Duct Flows. SAE Paper 881480, Oct. 1988.
22. Cosner, R.R.: Transonic Propulsion System Integration Analysis at McDonnell Aircraft Company. Transonic Symposium: Theory, Application, and Experiment, J.T. Foughner Jr., ed., NASA CP-3020, Vol. 1, Part 2, 1988, pp. 409-436.

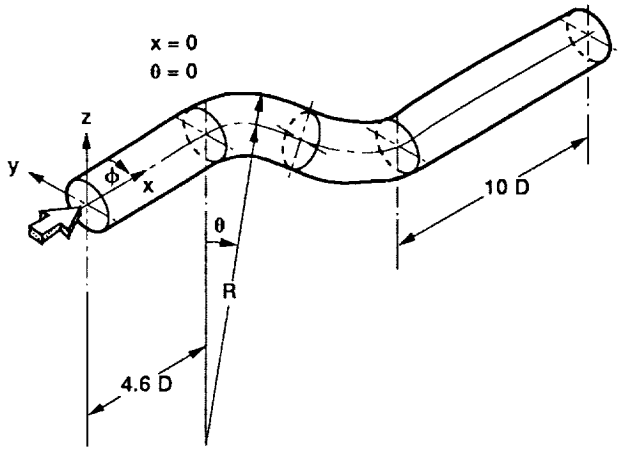

(a) Dimensions and coordinates.

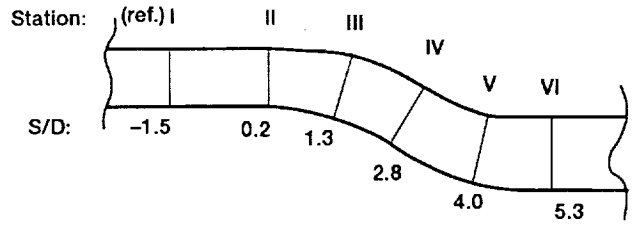

(b) Measurement stations.

Figure 1.—Coordinates and and measurement stations of the 30°-30°, nondiffusing S-duct. Duct inside diameter, 6.5 in.; mean radius of bends, 33 in.

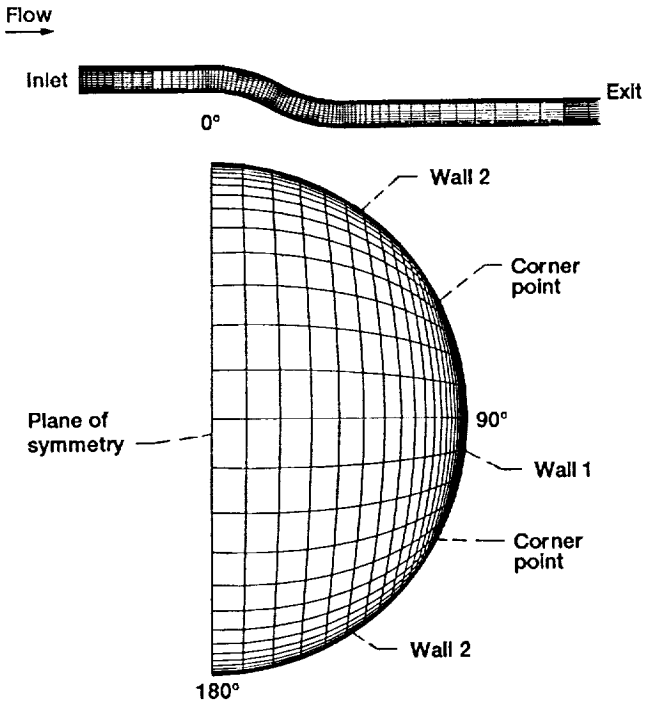

(a) H-grid; 75×33×33 mesh.

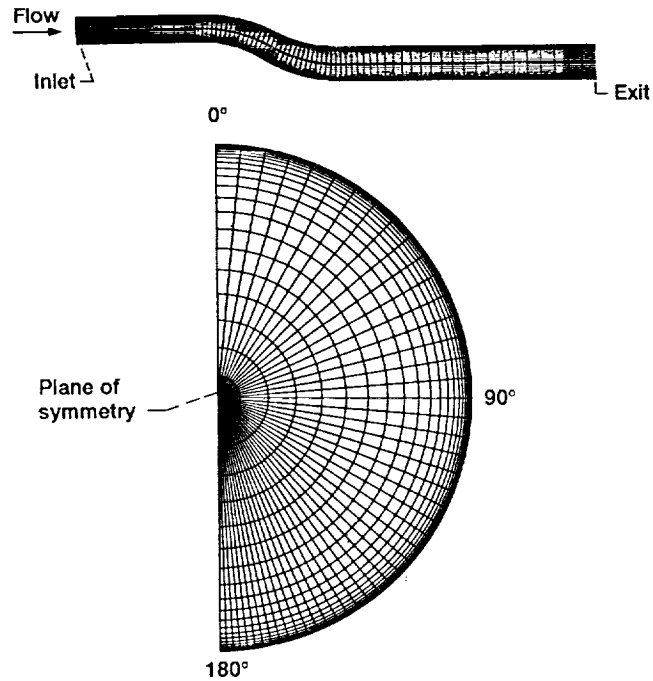

(b) O-grid; 75×35×31 mesh.

Figure 2.—Grid geometry for nondiffusing S-duct.

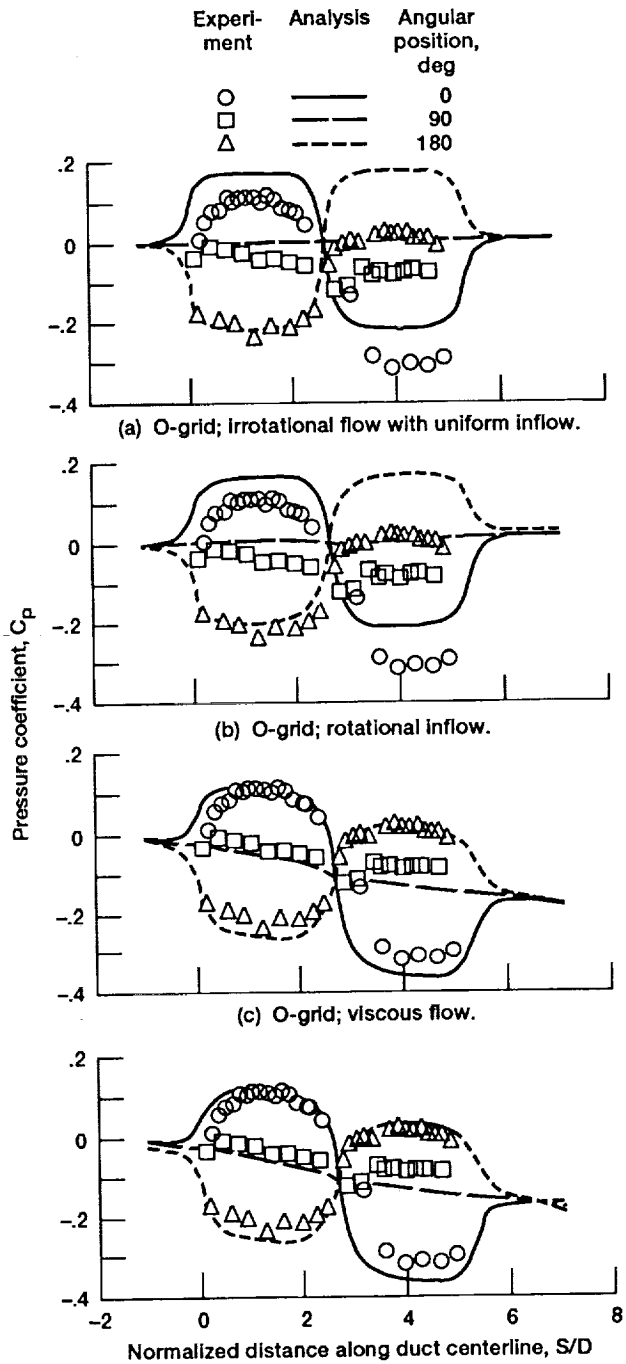

(a) O-grid; irrotational flow with uniform inflow.

(b) O-grid; rotational inflow.

(c) O-grid; viscous flow.

(d) H-grid; viscous flow.

Figure 3.—Surface pressure distributions.

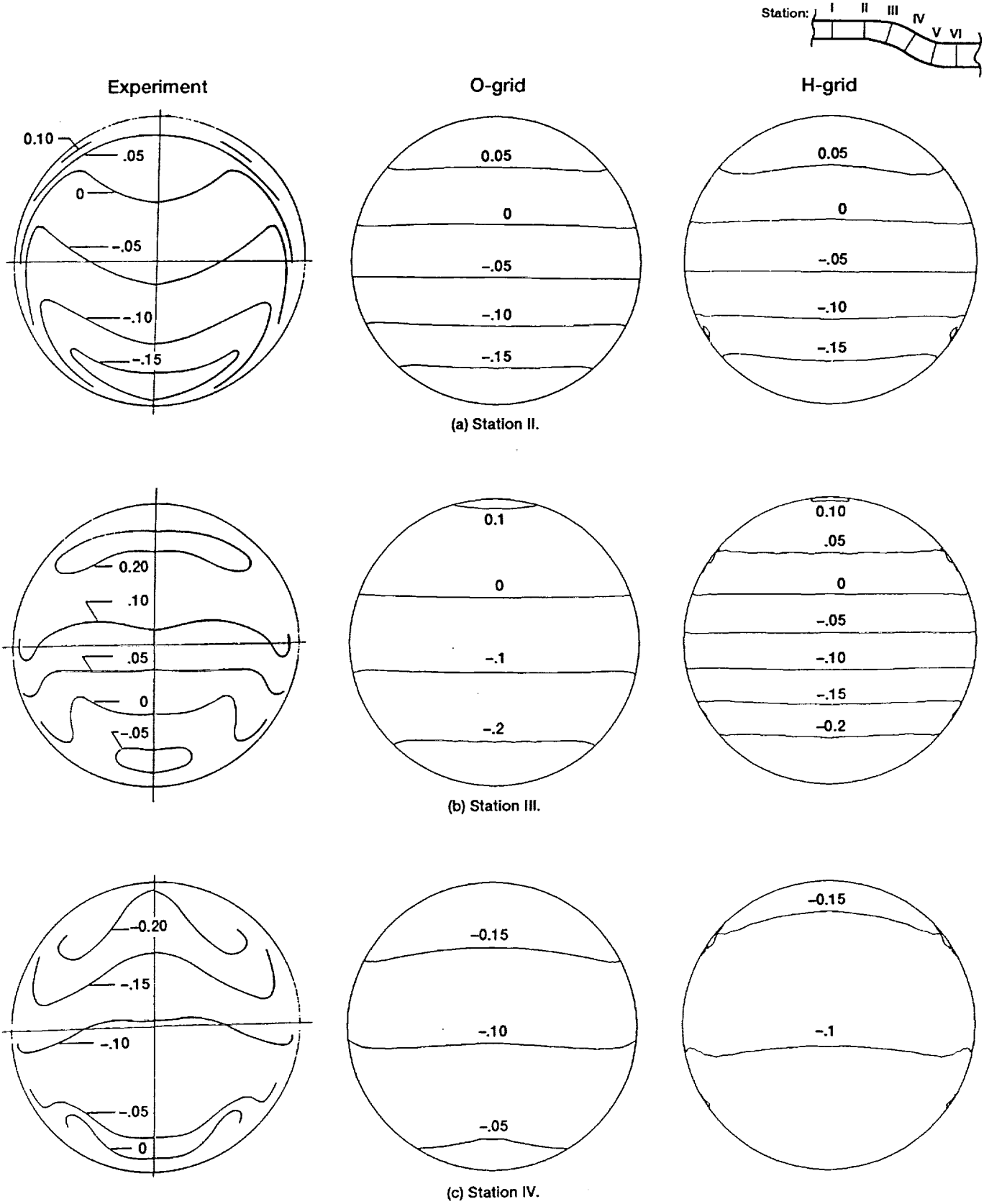

(a) Station II.

(b) Station III.

(c) Station IV.

Figure 4.—Contours of static pressure coefficient, $C_{p,s}$.

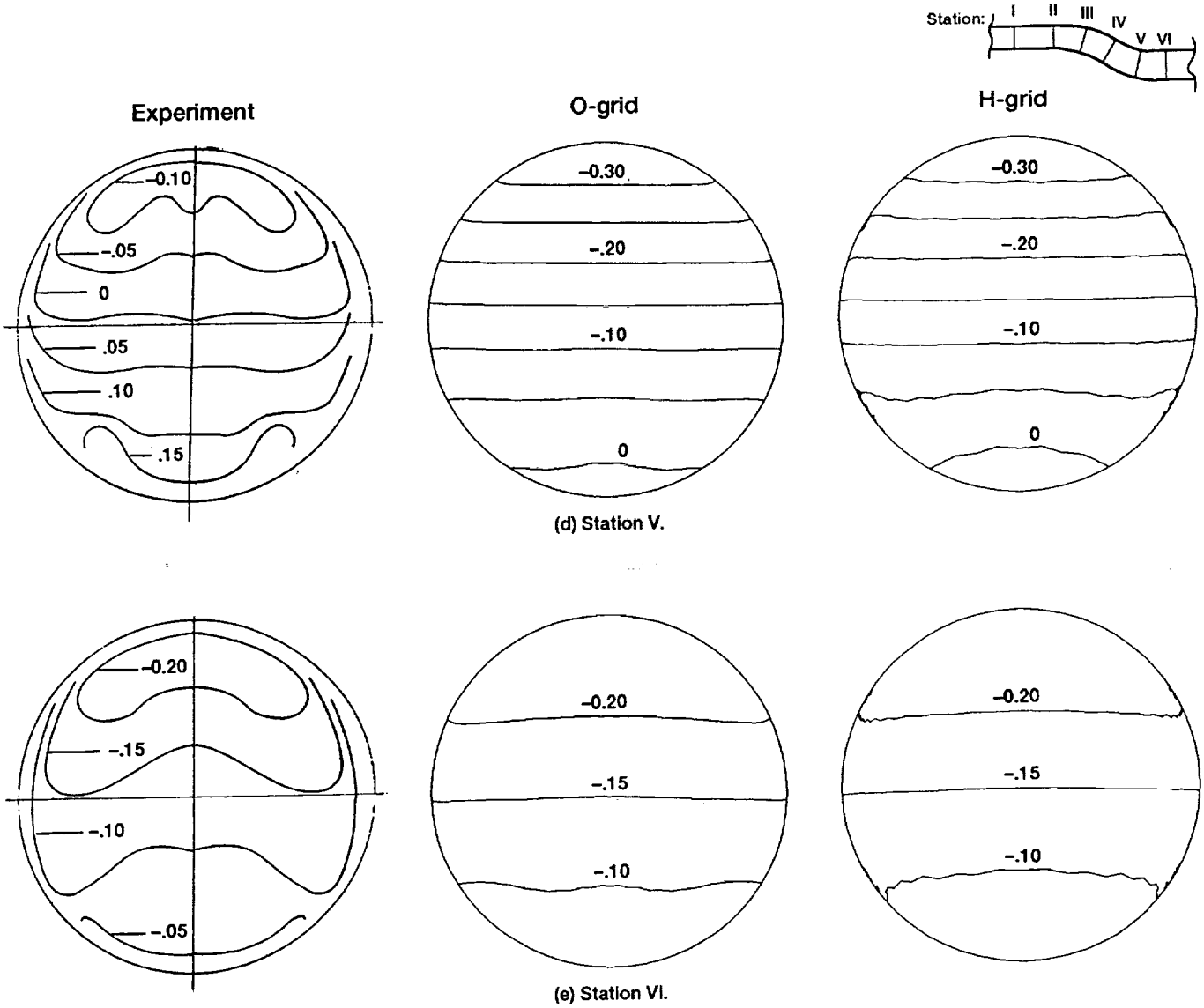

(d) Station V.

(e) Station VI.

Figure 4.—Concluded.

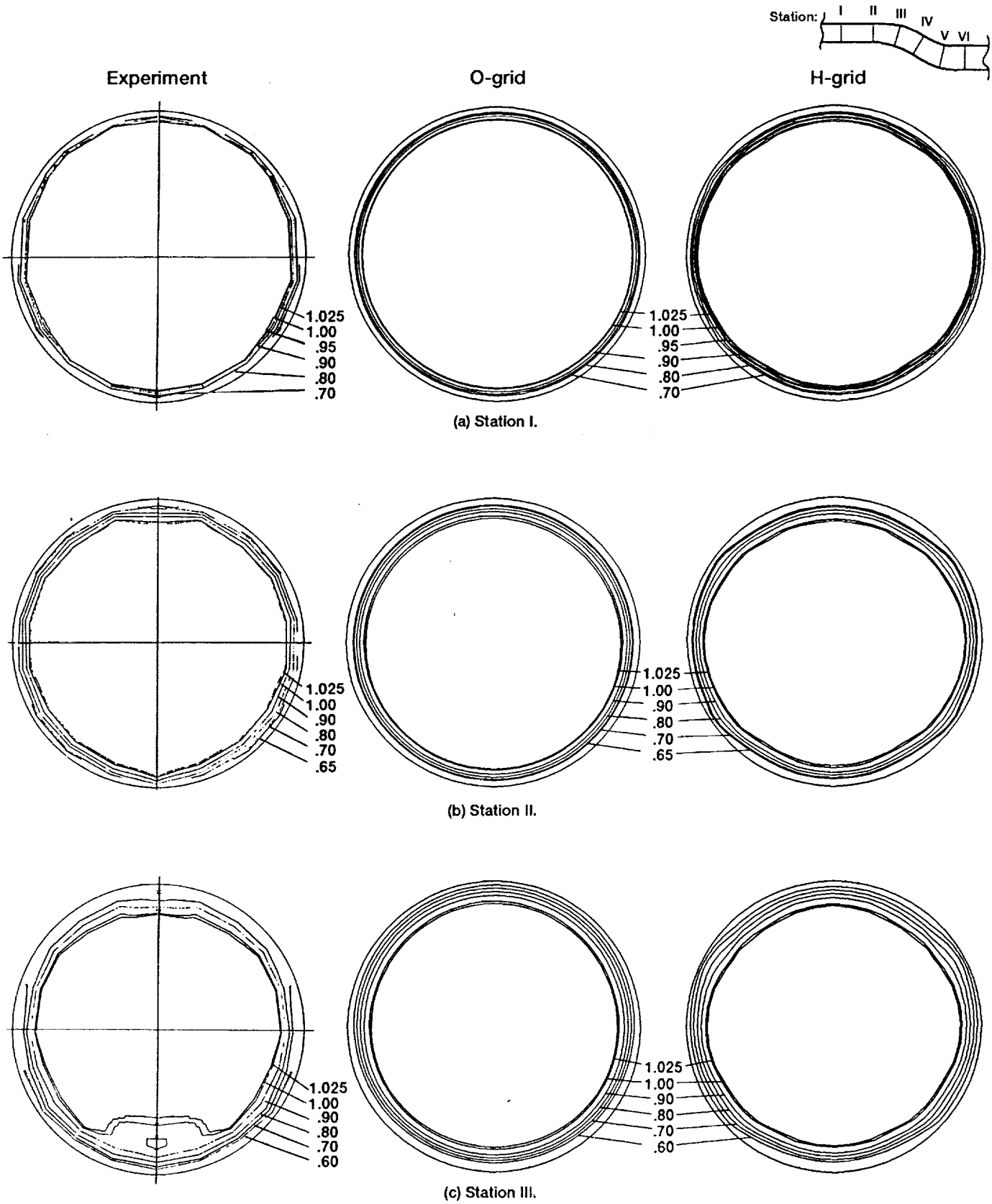

Figure 5.—Contours of total pressure .

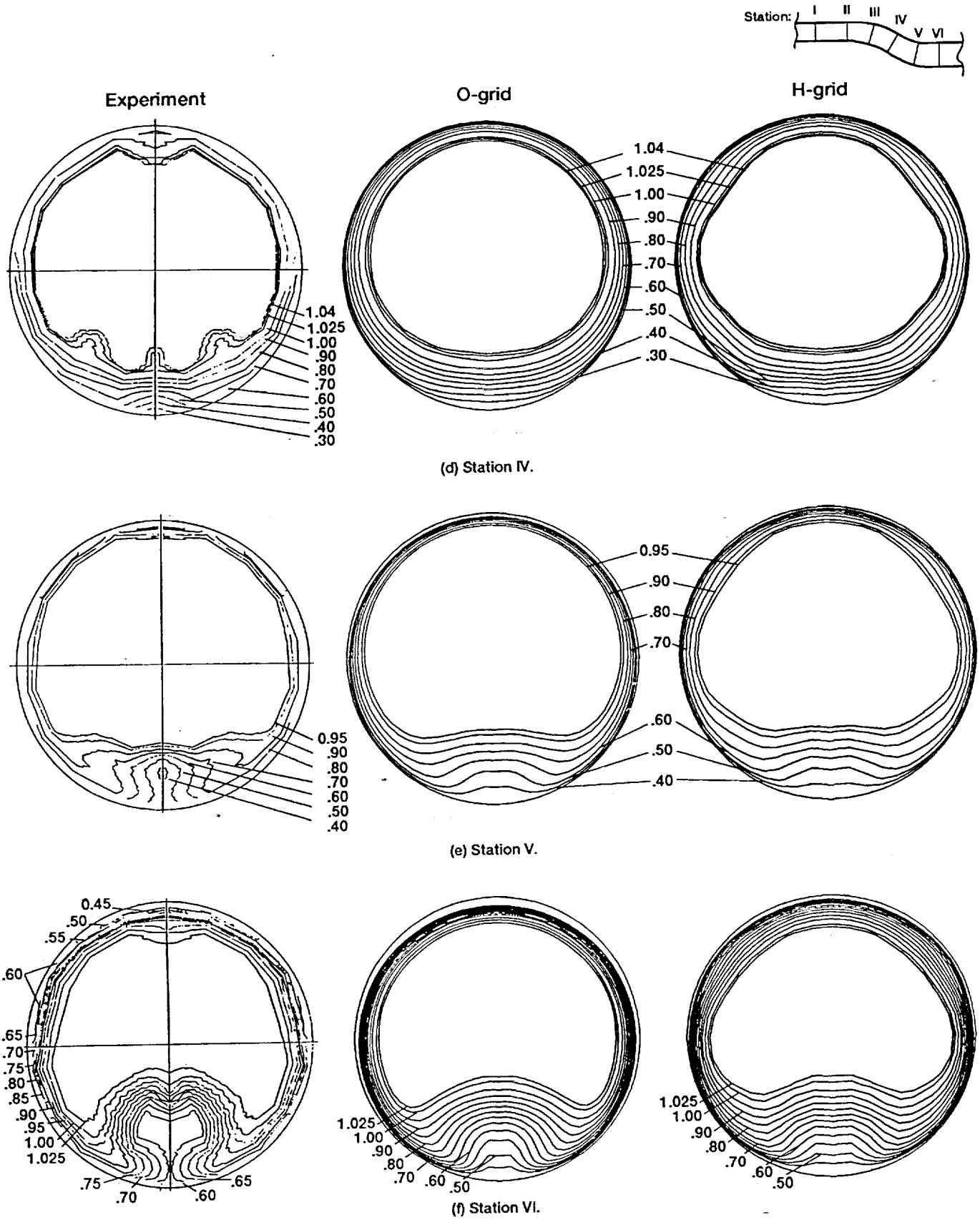

(d) Station IV.

(e) Station V.

(f) Station VI.

Figure 5.—Concluded.

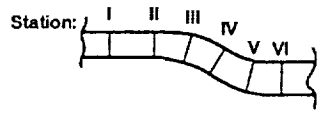

Experiment

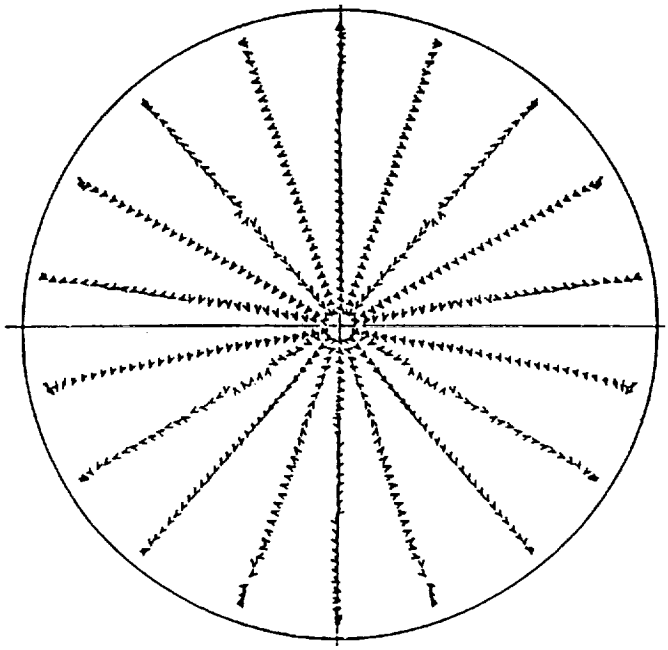

O-grid

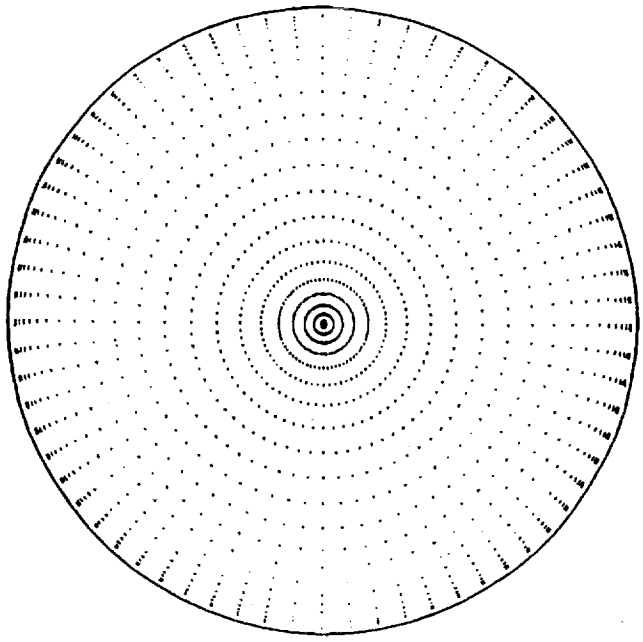

H-grid

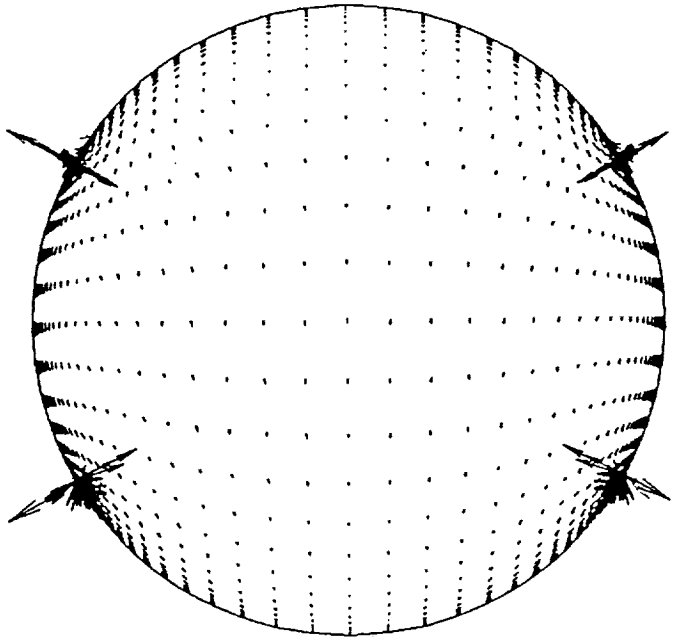

(a) Station II.

Figure 6.—Velocity vectors.

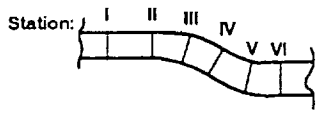

Experiment

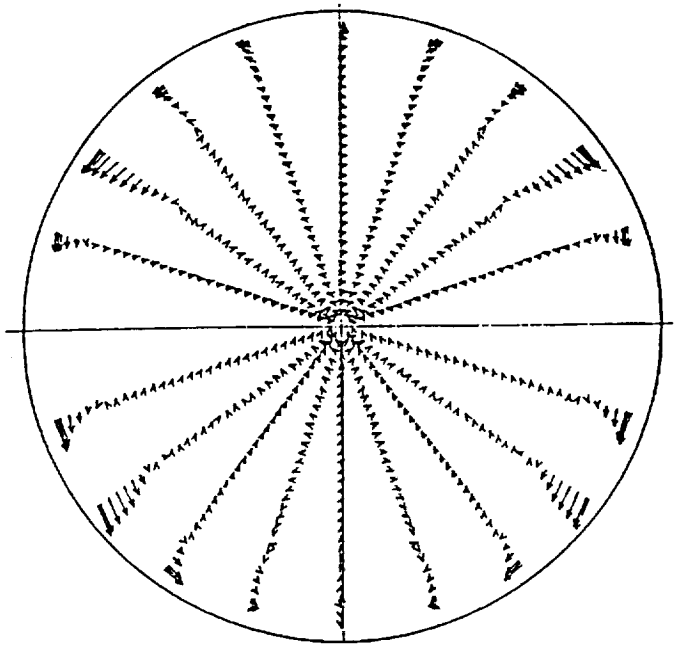

O-grid

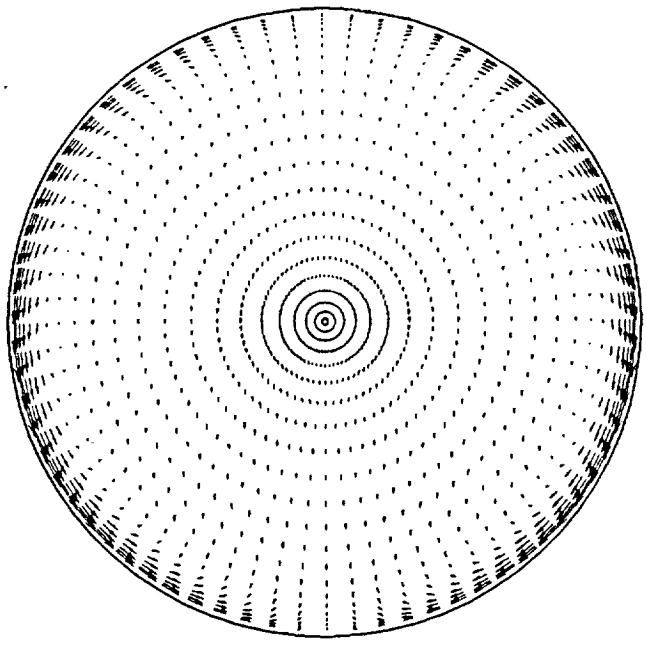

H-grid

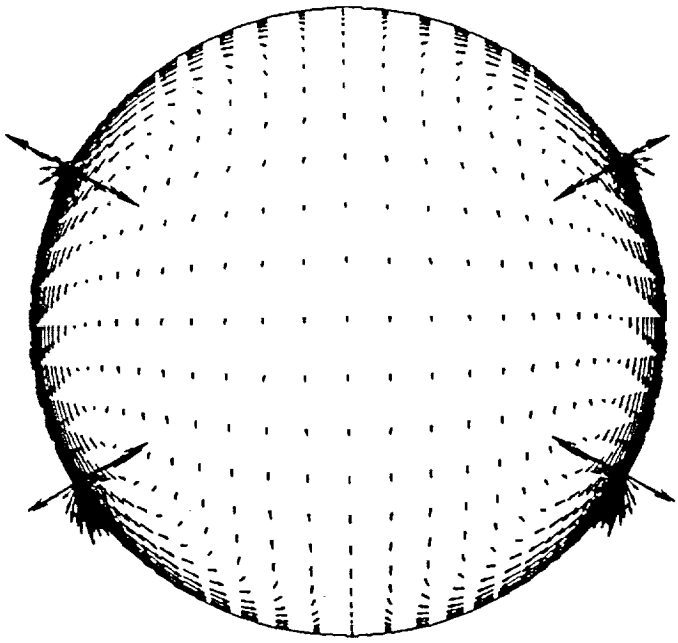

(b) Station III.

Figure 6.—Continued.

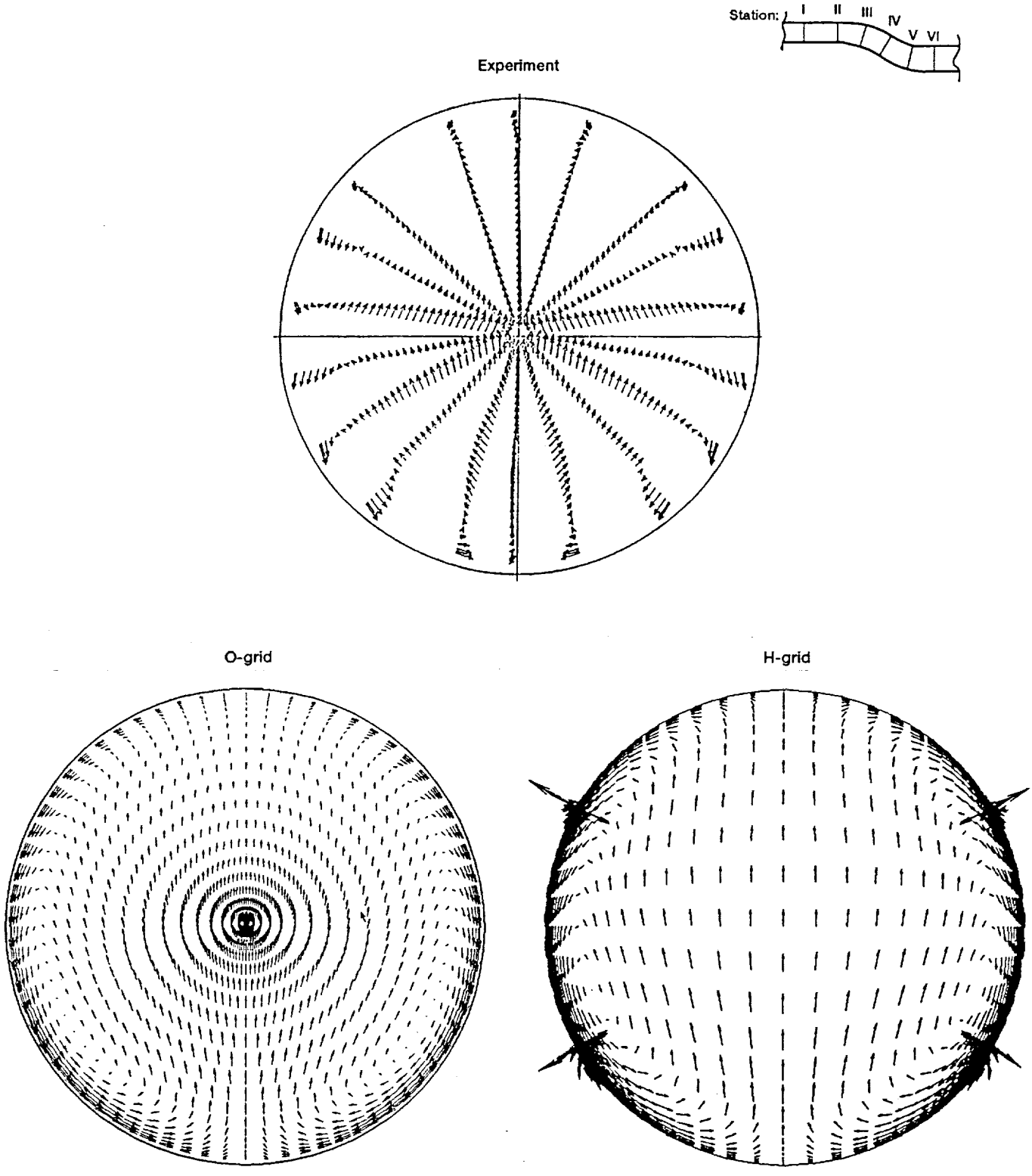

(c) Station IV.

Figure 6.—Continued.

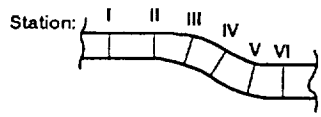

Experiment

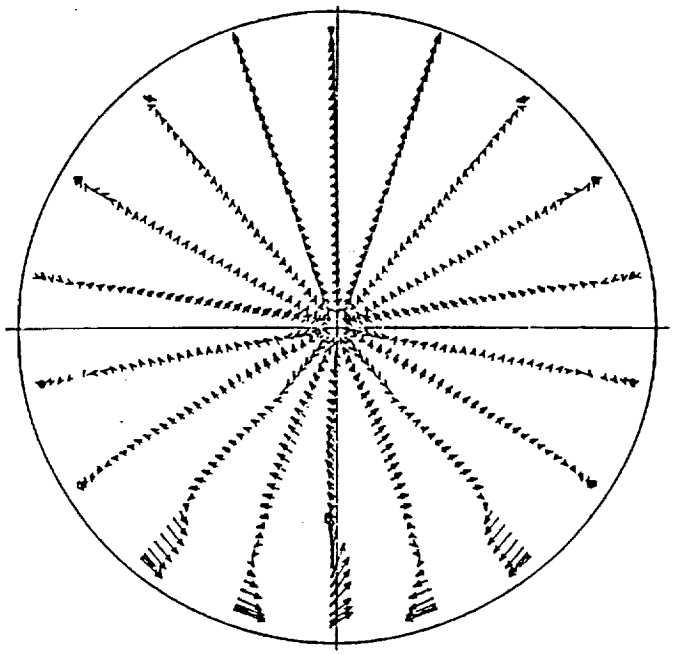

O-grid

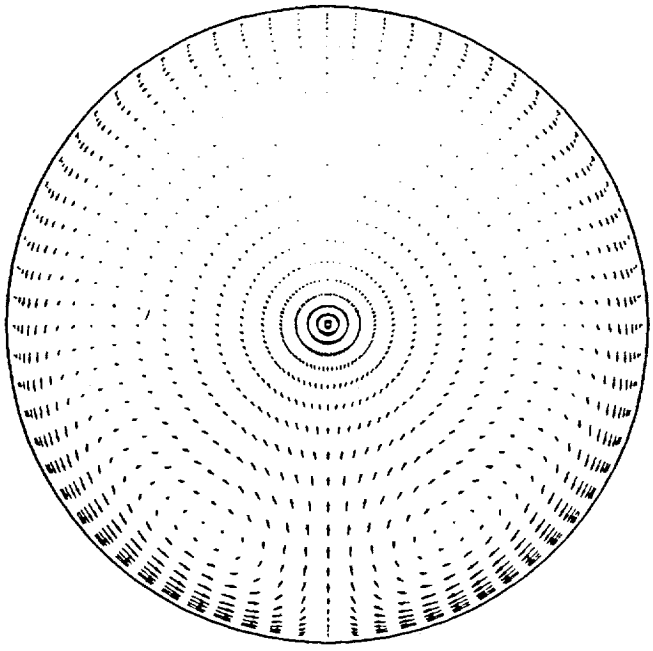

H-grid

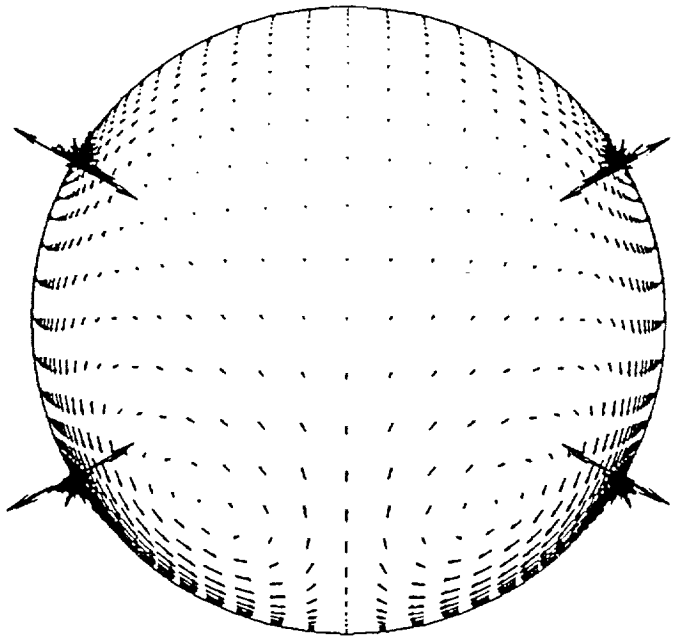

(d) Station V.

Figure 6.—Continued.

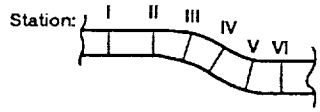

Experiment

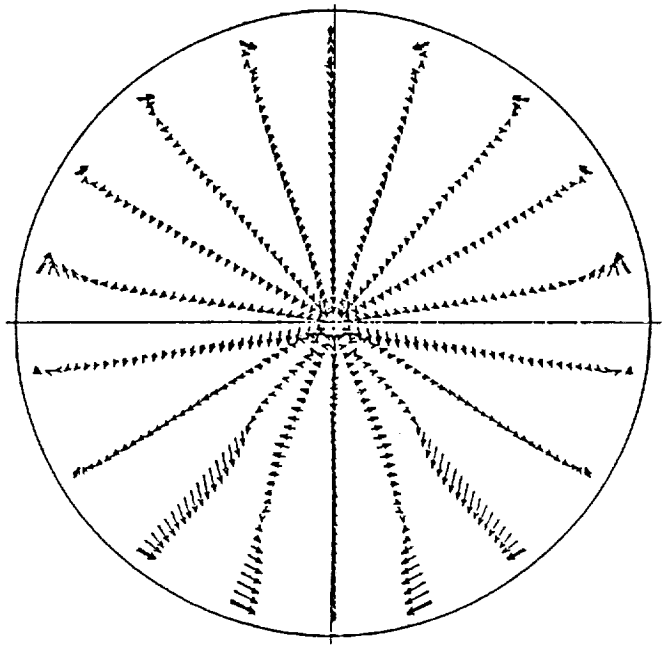

O-grid

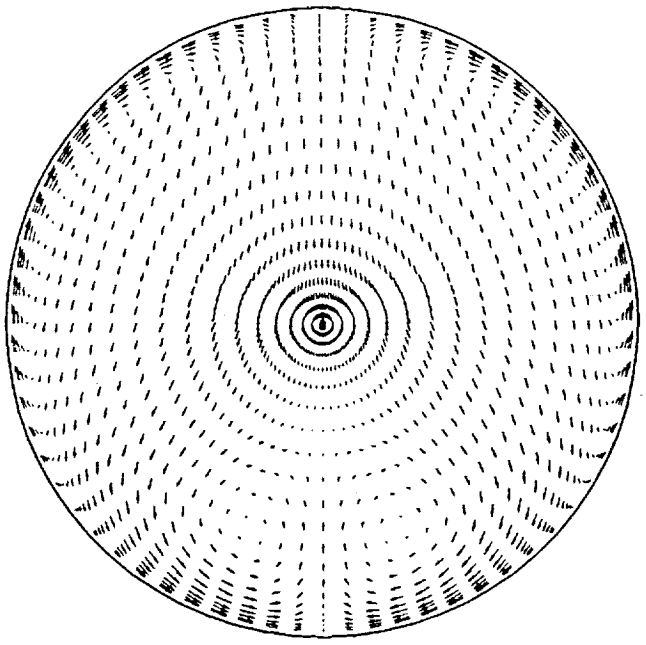

H-grid

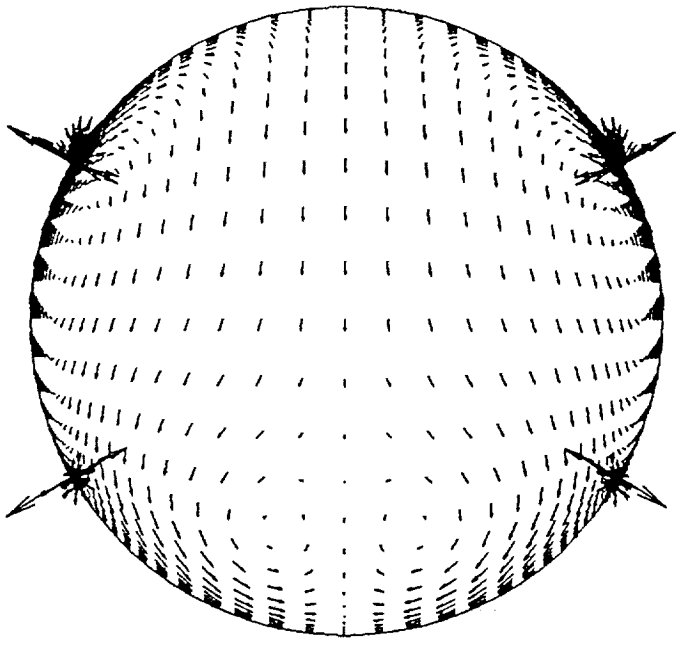

(e) Station VI.

Figure 6.—Concluded.

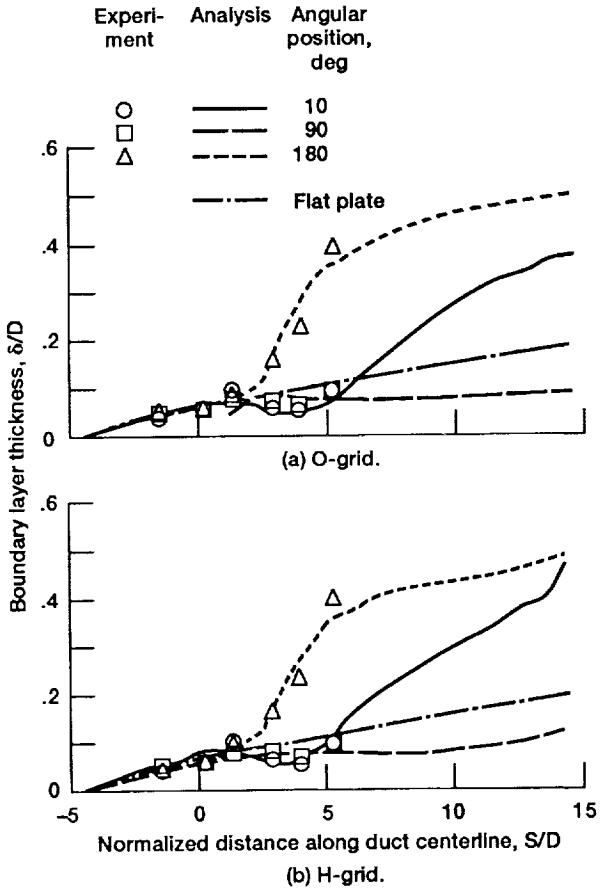

Figure 7.—Boundary layer growth.

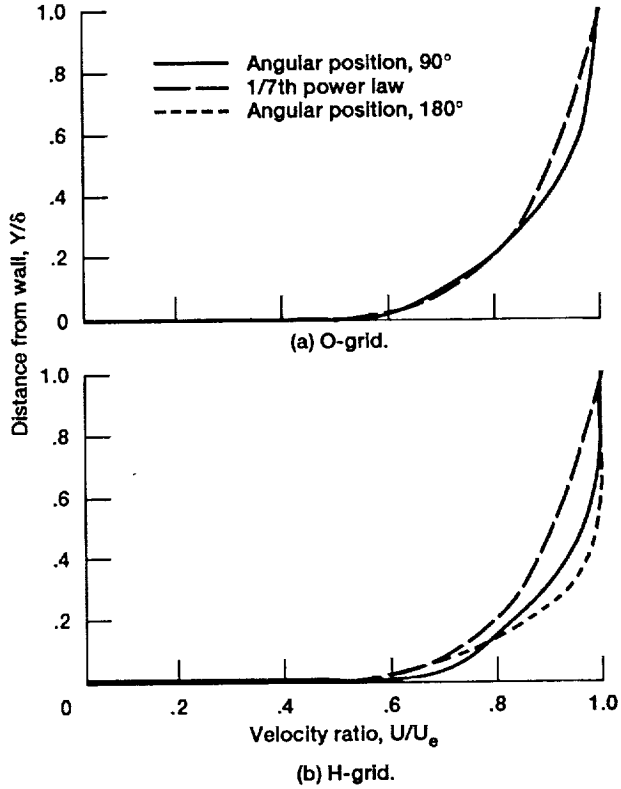

Figure 8.—Boundary layer profile at station I.

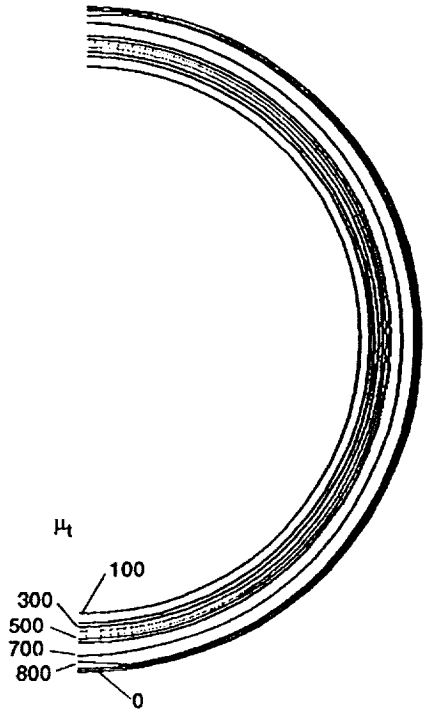

(a) O-grid.

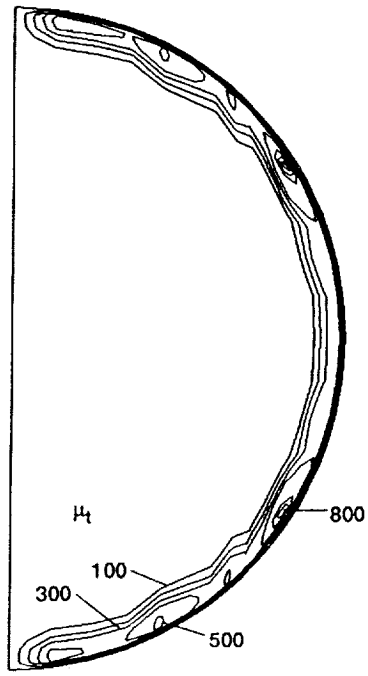

(b) H-grid.

Figure 9.—Turbulent viscosities at station I.

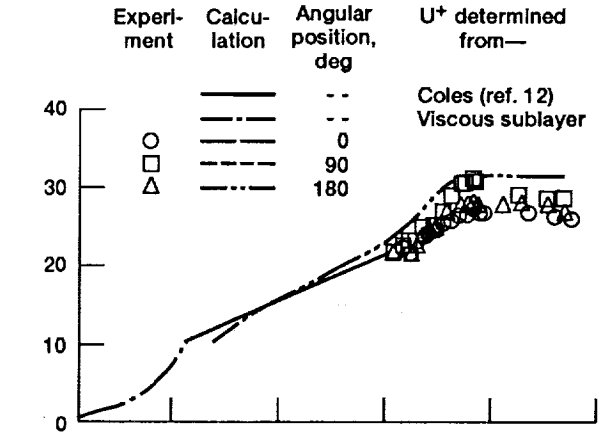

(a) Station I.

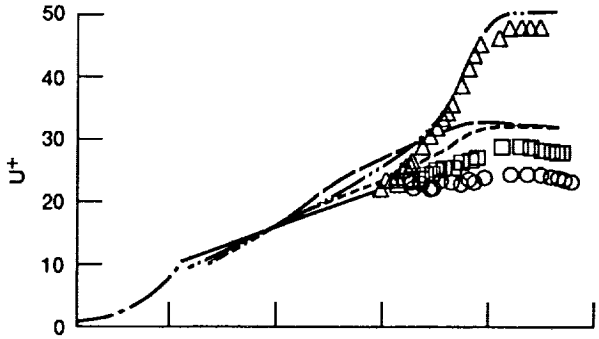

(b) Station IV.

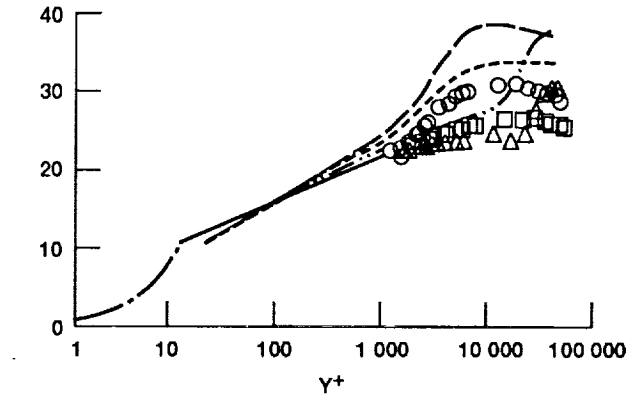

(c) Station VI.

Figure 10.—U^+ versus Y^+ for O-grid.

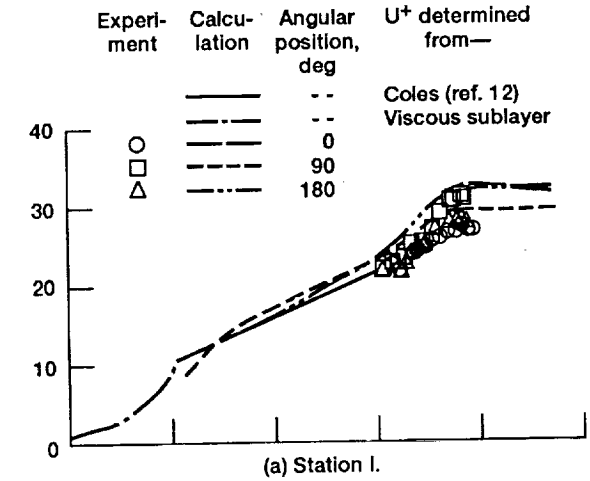

(a) Station I.

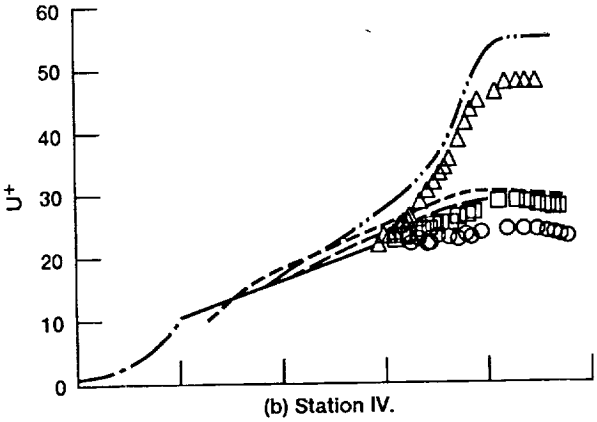

(b) Station IV.

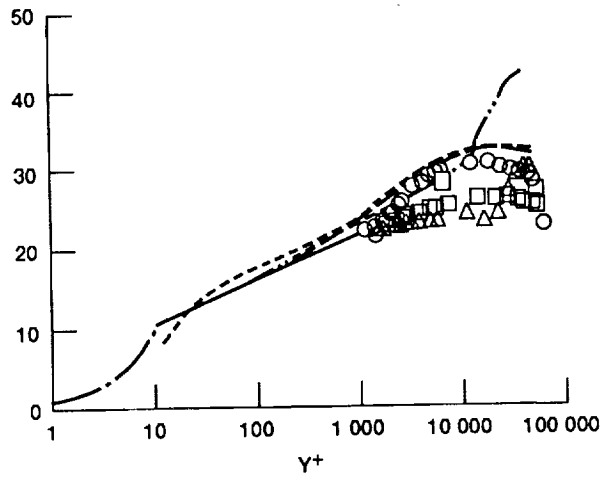

(c) Station VI.

Figure 11.—U+ versus Y+ for H-grid.

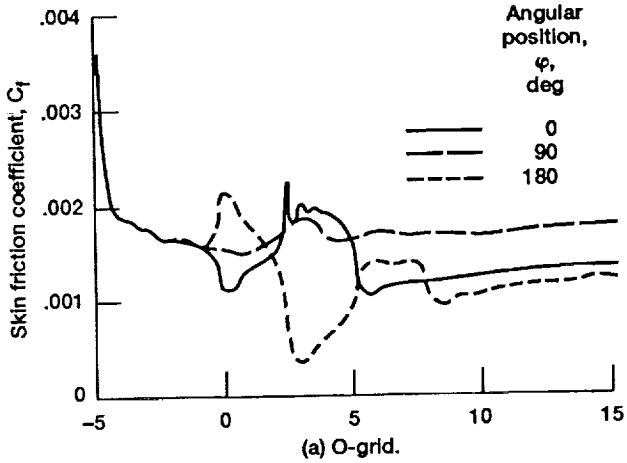

(a) O-grid.

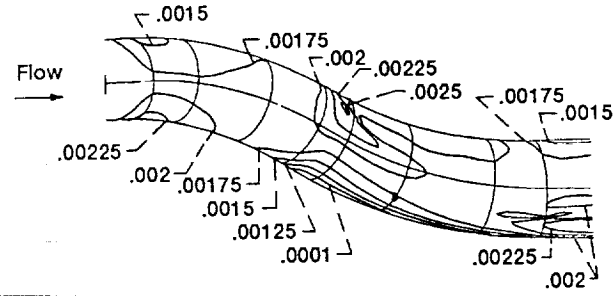

(b) Wall skin friction contours, o-grid.

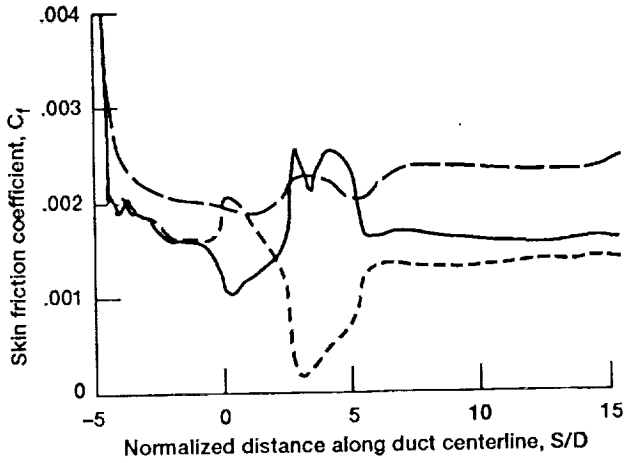

(c) H-grid.

Figure 12.—Coefficient of friction versus normalized distance along duct centerline.

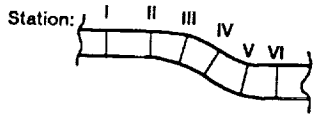

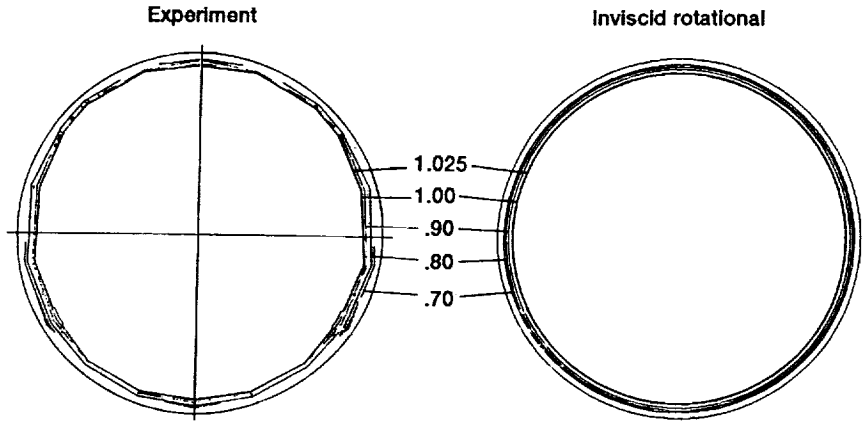

(a) Station I.

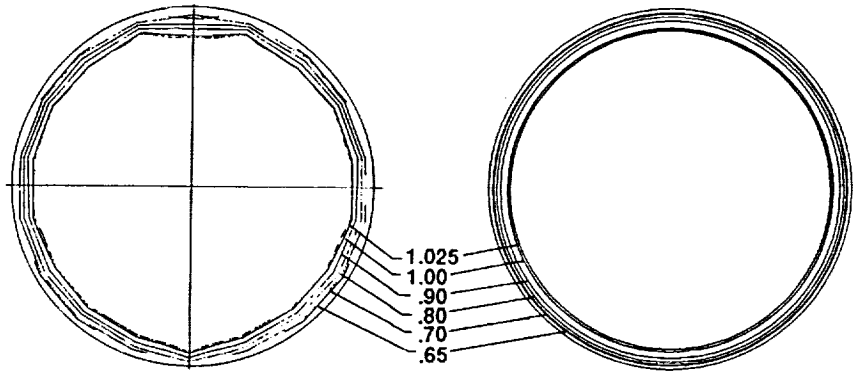

(b) Station II.

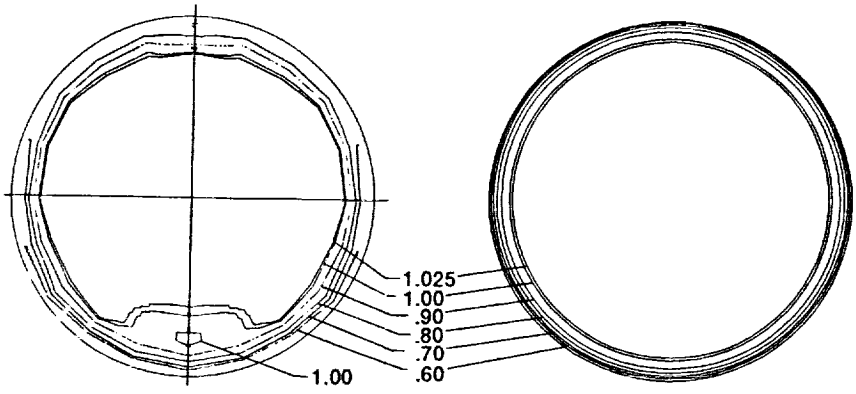

(c) Station III.

Figure 13.—Total pressure contours for inviscid, rotational flow flow; O-grid.

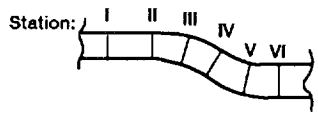

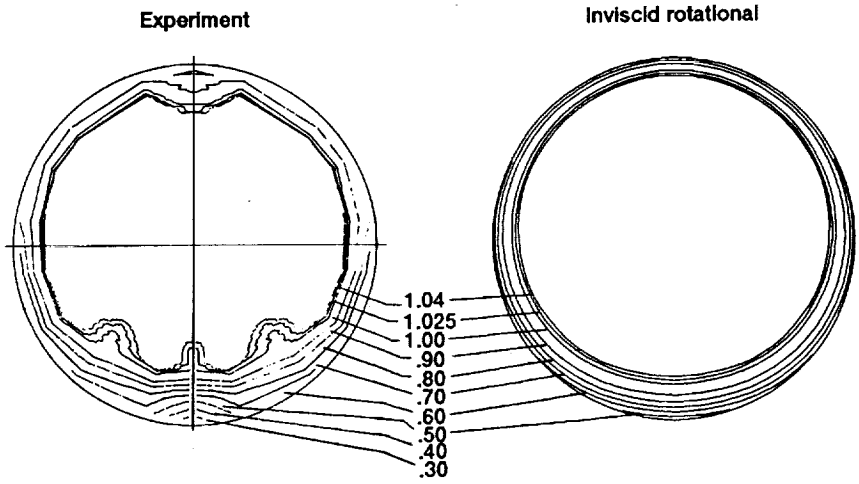

(d) Station IV.

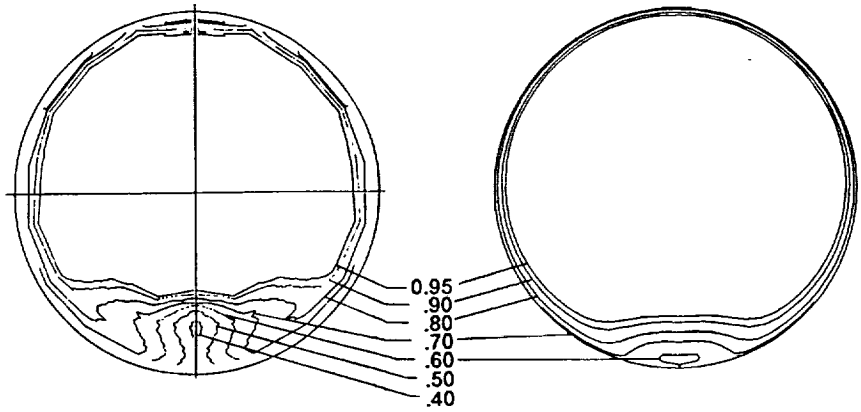

(e) Station V.

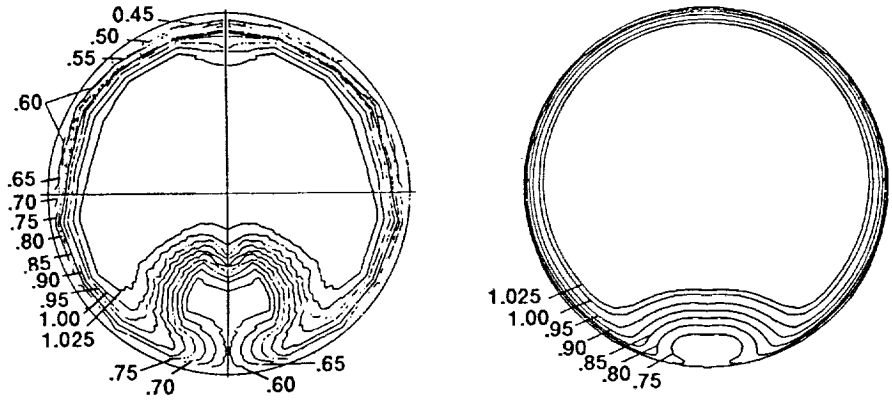

(f) Station VI.

Figure 13.—Concluded.

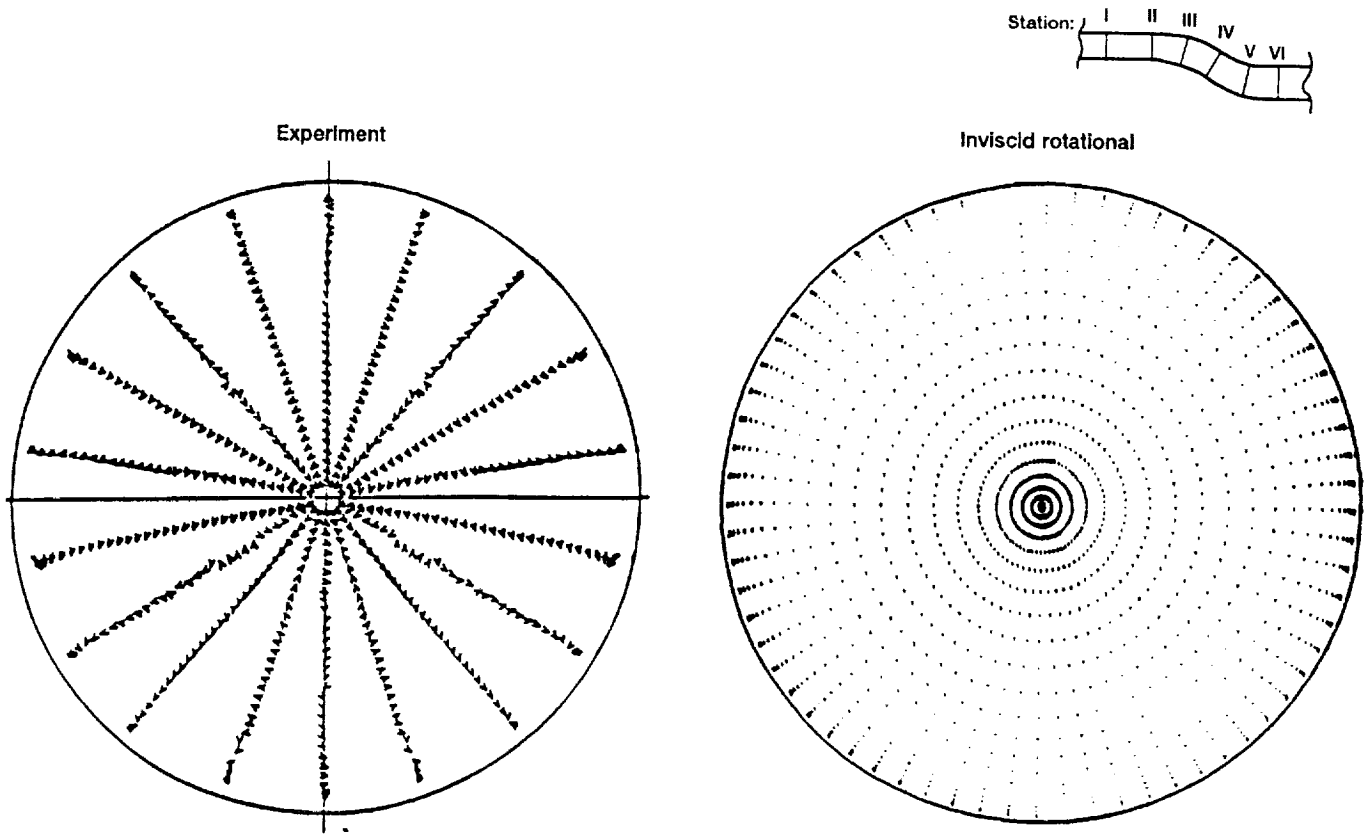

(a) Station II.

(b) Station III.

Figure 14.—O-grid.

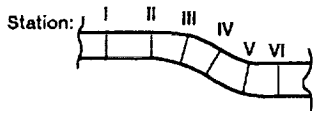

Experiment

Inviscid rotational

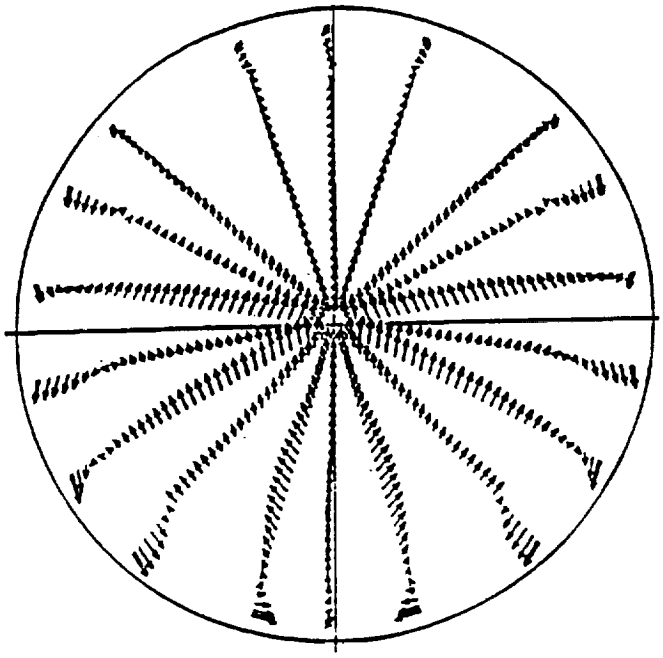

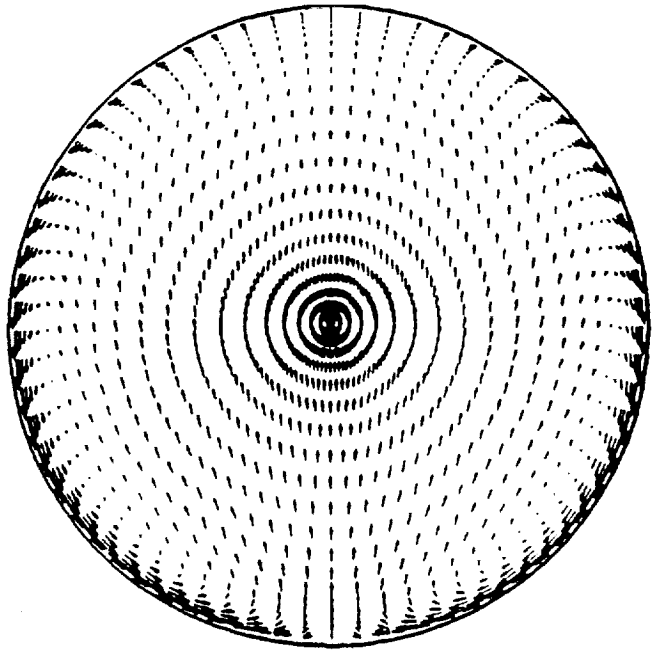

(c) Station IV.

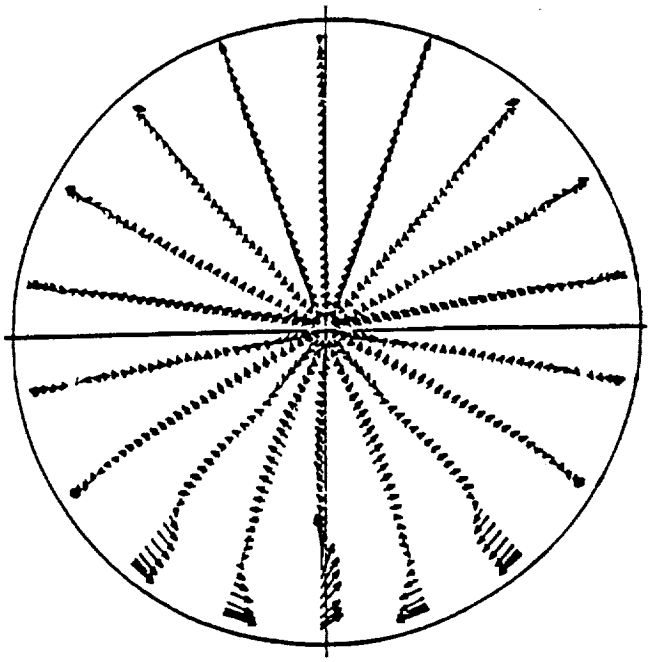

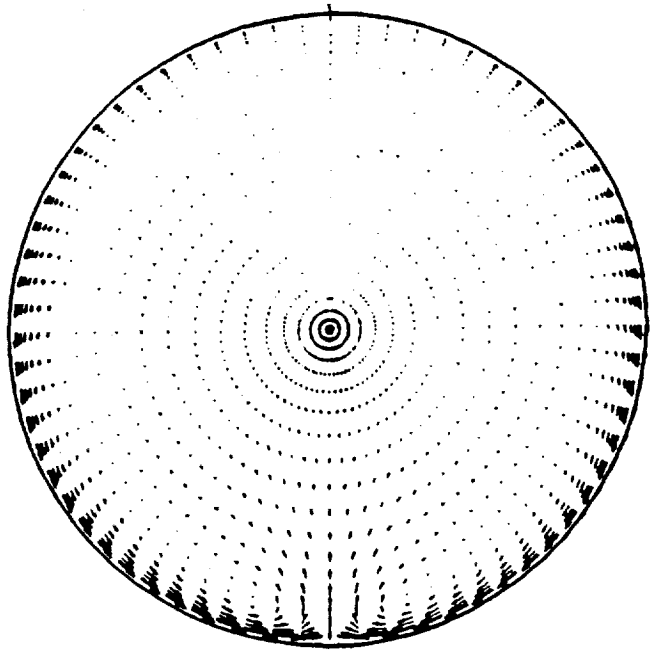

(d) Station V.

Figure 14.—Continued.

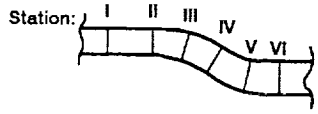

Experiment

Inviscid rotational

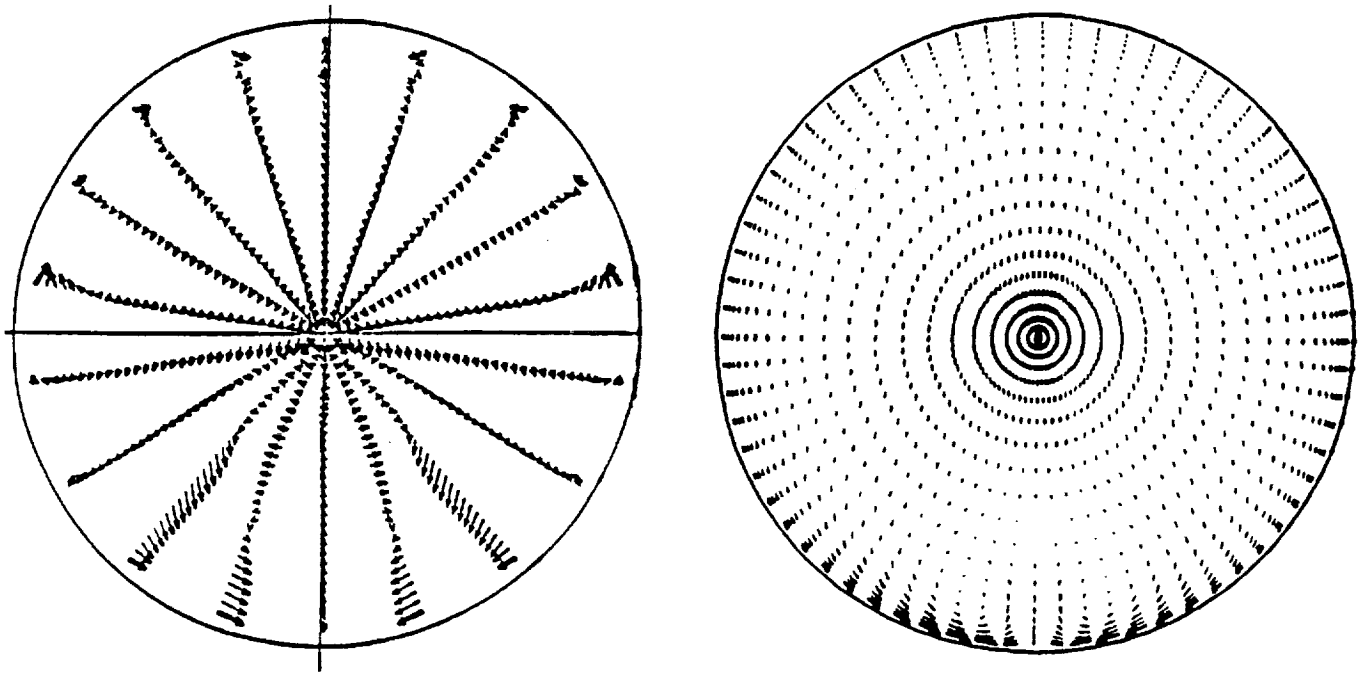

(e) Station VI.

Figure 14.—Concluded.

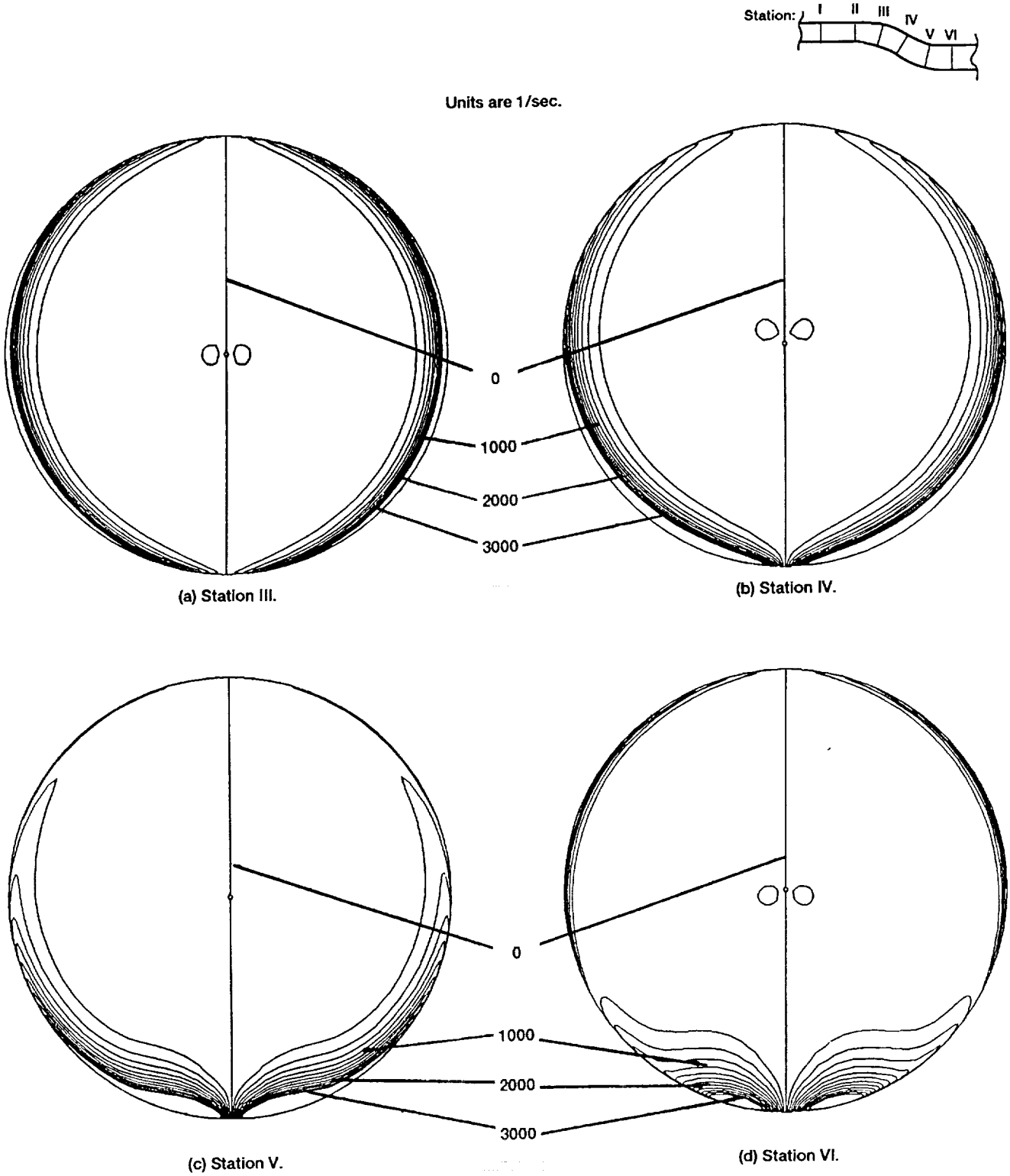

Figure 15.—Streamwise vorticity contours: Inviscid-rotational case. (Values shown are in units of reciprocal seconds).

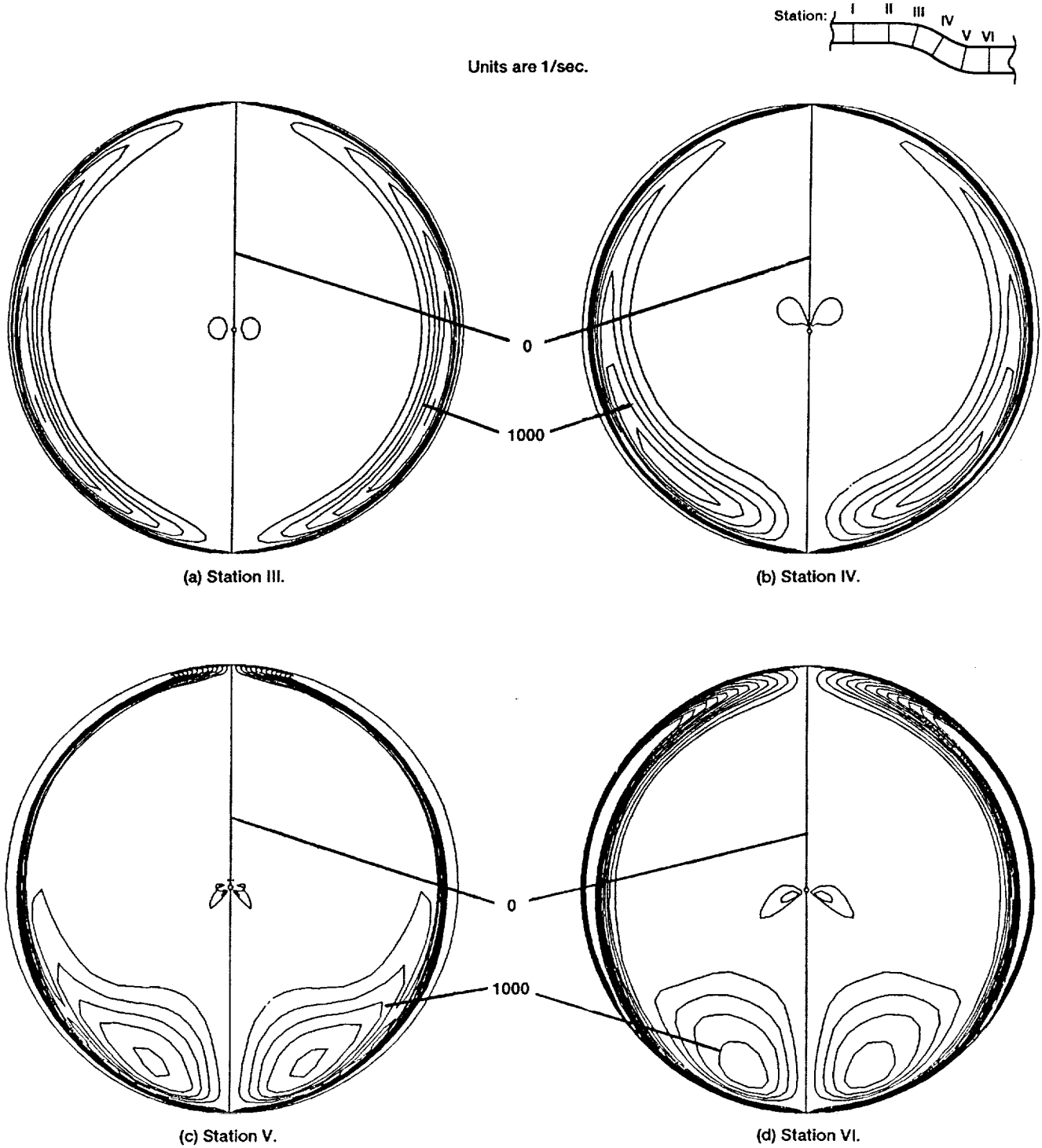

Figure 16.—Streamwise vorticity contours: fully turbulent case. (Values shown are in units of reciprocal seconds).

REPORT DOCUMENTATION PAGE

Form Approved
OMB No. 0704-0188

1. AGENCY USE ONLY (*Leave blank*)	2. REPORT DATE	3. REPORT TYPE AND DATES COVERED
	April 1992	Final Contractor Report

4. TITLE AND SUBTITLE

Three-Dimensional Compressible Turbulent Computations for a Nondiffusing S-Duct

5. FUNDING NUMBERS

WU-533-02-30
NAS3-25266

6. AUTHOR(S)

G.J. Harloff, J.R. DeBonis, C.F. Smith, and J.E. Bruns

7. PERFORMING ORGANIZATION NAME(S) AND ADDRESS(ES)

Sverdrup Technology, Inc.
Lewis Research Center Group
2001 Aerospace Parkway
Brook Park, Ohio 44142

8. PERFORMING ORGANIZATION REPORT NUMBER

None (E-6173)

9. SPONSORING/MONITORING AGENCY NAMES(S) AND ADDRESS(ES)

National Aeronautics and Space Administration
Lewis Research Center
Cleveland, Ohio 44135-3191

10. SPONSORING/MONITORING AGENCY REPORT NUMBER

NASA CR-4391

11. SUPPLEMENTARY NOTES

Project Manager, Robert E. Coltrin, Propulsion Systems Division, NASA Lewis Research Center. Responsible person, G.J. Harloff, (216) 826-6683.

12a. DISTRIBUTION/AVAILABILITY STATEMENT

Unclassified - Unlimited
Subject Category 02

12b. DISTRIBUTION CODE

13. ABSTRACT (*Maximum 200 words*)

The PARC3D code was used to compute the compressible turbulent flow within a three-dimensional nondiffusing S-duct. The present study provides a frame of reference for future computational fluid dynamic studies of internal flows with strong secondary flows and provides an understanding of the performance characteristics of a typical S-duct with attached flow. The predicted results, obtained with both H- and O-grids, are compared with the experimental wall pressures, static- and total-pressure fields, and velocity vectors. Additionally, computed boundary-layer thickness, velocity profiles in wall coordinates, and skin friction values are presented.

14. SUBJECT TERMS

Computational fluid dynamics; Ducts; Ducted flow; Turbulent flow

15. NUMBER OF PAGES

32

16. PRICE CODE

A03

17. SECURITY CLASSIFICATION OF REPORT	18. SECURITY CLASSIFICATION OF THIS PAGE	19. SECURITY CLASSIFICATION OF ABSTRACT	20. LIMITATION OF ABSTRACT
Unclassified	Unclassified	Unclassified	

NSN 7540-01-280-5500

Standard Form 298 (Rev. 2-89)
Prescribed by ANSI Std. Z39-18
298-102

NASA-Langley, 1992